Coupling effects of temperature and strain rate on the mechanical behavior and multiple deformation mechanisms of an equiatomic refractory high-entropy alloy

Xinrong Song [a, b], Jianjun Wang [a, b, *], Xiangxiang Tu [a, b], Xueyao Hu [c], Dan Zhao [a, b], Shengguo Ma [a, b], Zhiming Jiao [a, b], Tuanwei Zhang [a, b], Wei Wen [d], Zhihua Wang [a, b, *]

[a] Institute of Applied Mechanics, College of Aeronautics and Astronautics, Taiyuan University of Technology, Taiyuan 030024, PR China

[b] Shanxi Key Laboratory of Material Strength and Structural Impact, Taiyuan University of Technology, Taiyuan 030024, PR China

[c] Xi'an Modern Chemistry Research Institute, Xi'an, Shaanxi 710065, PR China

[d] School of Engineering, Lancaster University, Lancaster, LA1 4YW, UK

Acknowledgments

This work was supported by the National Natural Science Foundation of China (Grant Numbers: 12172245, 12225207, and 12372364)

[*] Corresponding author.
E-mail addresses: wangjianjun@tyut.edu.cn (Jianjun Wang), wangzh@tyut.edu.cn (Zhihua Wang)

Abstract

The extraordinary high-temperature strength of refractory high-entropy alloys makes them promising candidates for critical engineering applications in extreme service environments, particularly under combined high temperature and high strain rate loading conditions. This study investigated the coupling effects of temperature (293 K – 1273 K) and strain rate (10^{-3} s^{-1} – 3000 s^{-1}) on the mechanical behavior and deformation mechanisms of an equiatomic TiZrNbVTa refractory high-entropy alloy with a single body-centered cubic structure. It shows an exceptional combination of strength and ductility within the selected temperature and strain rate ranges. Microstructural analysis revealed that multiple deformation mechanisms including severe lattice distortion, kink band, stress-induced martensite transformation from body-centered cubic to omega phase, and third-type strain aging are prevalent during deformation over the wide range of temperatures and strain rates, significantly enhancing strength-ductility performance of the alloy particularly under extreme conditions. The third-type strain aging occurred at different strain rates, which shifts to a higher temperature range as strain rate increases. Zr atoms acting as "solute atoms" form short-range clusters, thereby pinning the moving dislocations. Finally, a deformation mechanism map was proposed over a wide range of temperatures and strain rates. This study provides insight into the design of refractory high-entropy alloys for extreme thermos-mechanical applications.

Keywords: Refractory high-entropy alloy; Temperature; Strain rate; Microstructure evolution; Kink band; Stress-induced martensitic transformation

Article Highlights

- Compression behavior of TiZrNbVTa RHEA was studied at various temperatures and strain rates.
- The third-type strain aging was attributed to the formation of Zr-enriched short-range clusters.

- A deformation mechanism map was proposed.

1. Introduction

Utilizing a single principal element and other alloying elements with dilute concentrations to optimize the material properties of interest has been anchored over centuries. For decades, the conventional design strategy has shifted towards a focus on multi-component compositional spaces, termed multi-component element alloys (MPEAs) or most commonly, high-entropy alloys (HEAs), which are typically defined as equiatomic or near-equiatomic systems forming simple disordered solid solutions [1, 2]. HEAs have unique combinations of properties that are not achievable in conventional alloys, including high strength and hardness [3-5], superior ductility and damage tolerance [6-8], good fatigue resistance [9, 10], excellent resistance to dynamic loading [11, 12], outstanding corrosion and oxidation resistance [13-15], strong wear resistance [16-18], and attractive biocompatibility [19, 20]. In 2010, Senkov et al. [21-23] first introduced refractory elements into HEAs and proposed the concept of refractory HEAs (RHEAs). RHEAs are typically composed of stable solid solutions with high configurational entropy, and they usually form a single body-centered cubic (BCC) structure [24-26]. The demand for materials with great thermal stability and temperature insensitive properties has driven the advancement of the RHEAs [27, 28].

Recent studies [29-33] have indicated that the yield strength of RHEAs is sensitive to strain rates during plastic deformation at room and elevated temperatures. At room temperature, the strength of the TiZrNbTa RHEA increases significantly with increasing strain rate, as the yield strength at a high strain rate (6500 s^{-1}) is twice that at a low strain rate (10^{-3} s^{-1}) [31]. It was found that the formation of Zr-enriched local chemical orderings (LCOs) facilitates dislocation slip, enhancing homogeneous deformation capacity and adiabatic shear resistance under high strain rates [31]. The deformation of a quinary TaNbHfZrTi RHEA reveals the existence of coupling effects between strain rates and temperatures on the microstructure evolution, exhibiting an increase in strain rate sensitivity with increasing temperature [34]. Dirras et al. [35]

reported that the deformation of the TaNbHfZrTi RHEA under dynamic compression was strongly localized within macroscopic shear bands, which were accompanied by softening even after the onset of yielding, whereas deformation at low strain rates was characterized by continuous hardening.

Based on the active deformation mechanism, flow stress vs. strain rate plot sequentially displays two distinct regimes within the strain rates ranging from 1 s^{-1} to 10^4 s^{-1}, i.e., the thermally active regime and the viscous drag regime [35-38]. The transition between the two mechanisms manifests at a strain rate of approximately 10^3 s^{-1} [39, 40]. Microstructurally, some RHEAs exhibit multiple deformation mechanisms at strain rates exceeding 10^3 s^{-1}, including multiple slip of dislocations, and, in extreme, deformation twinning [31, 35, 41, 42]. Deformation temperature is another key factor influencing the mechanical behavior of RHEAs. At room temperature, plastic deformation in RHEAs is primarily governed by 1/2<111> screw dislocations [43-45], whereas at elevated temperatures, it is mainly dominated by edge dislocations [46, 47]. Although some studies have focused on the mechanical properties and deformation mechanisms of RHEAs under different temperatures or strain rates, the coupling effects of temperature and strain rate on the mechanical properties and deformation behavior of RHEAs need further exploration.

In this work, an equiatomic TiZrNbVTa RHEA with a single BCC phase was prepared. The uniaxial quasi-static and dynamic compression tests of the RHEA were performed over a wide temperature range (293 K – 1273 K). The coupling effects of temperature and strain rate on the mechanical response of the RHEA were studied in detail. Furthermore, the microstructure evolution and deformation mechanisms of the TiZrNbVTa RHEA were analyzed and discussed based on the experimental results.

2. Materials and experimental details

2.1 Material preparation

The equiatomic TiZrNbVTa RHEA was manufactured by induction skull melting (ISM) using the mixture of Ti, Zr, Nb, V, and Ta elements with high purity (> 99.9 wt. %) under an argon atmosphere. To ensure the compositional homogeneity of the RHEA, the ingot was re-melted five times. The as-cast ingot was annealed at 1473 K for 12 h in vacuum to eliminate the microscopic segregation, followed by water cooling. The cylindrical samples were obtained by wire cutting with a diameter of 5 mm and length of 5 mm. The ends of each sample were mechanically polished with 800 grit and 4000 grit sandpapers and then lubricated by the molybdenum-powder to reduce the end friction during compression deformation.

2.2 Microstructure characterization

The initial crystal structure of the RHEA after the homogenization treatment was characterized by X-ray diffraction (XRD) using a Rigaku Ultima IV diffractometer operated at 45 kV and 40 mA. The XRD source was Cu-Kα radiation (λ = 1.5406 Å) in the 2θ range from 20° to 80° with the scanning rate of 4°/min. A JSM-IT700HR filed-emission scanning electron microscope (FE-SEM) equipped with an electron backscatter diffraction (EBSD) detector operated at 20 kV was used for EBSD measurements. Transmission electron microscopy (TEM, JEOL JEM2100F) analysis was carried out at an acceleration voltage of 200 kV. The samples for EBSD were mechanically ground and polished, and followed by argon ion-beam cross-section polishing (CP) to remove residual stress on the sample surface. The samples for TEM were mechanically ground to about 50 μm thick with a diameter of 3 mm and then prepared by ion milling. The sample for TEM were mechanically ground to about 50 μm thickness with a diameter of 3 mm using grit silicon carbide papers. After mechanical thinning, ion milling was carried out using a Gatan 695 system at 5 keV (± 8°) until perforation, followed by a gradual reduction in energy and angle down to 3

keV (± 3°) for 5 min to reduce thermal damage and surface amorphization. In order to avoid oxidation, prepared TEM samples were kept in a vacuum container for less than one day prior to observation.

2.3 Mechanical experiments

2.3.1 Quasi-static compression experiments

The quasi-static experiments were conducted with a strain rate of 10^{-3} s^{-1} and temperatures ranging from 293 K to 1273 K using universal testing machine. To provide the required temperatures during elevated temperature experiments, a silicon molybdenum radiant-heating furnace was used. Temperatures for the experiments were measured using thermocouple arrangement and controlled constant within ± 3 K. Each sample was heated up to the required temperature at a rate of 10 K/s, and then kept for 3 minutes to ensure the temperature uniformity before loading. The samples were immediately water quenched after hot deformation to preserve their deformed microstructure.

2.3.2 Dynamic compression experiments

The dynamic experiments were conducted at strain rates of 1×10^{3} s^{-1} and 3×10^{3} s^{-1} using an enhanced split Hopkinson pressure bar (SHPB) system. The experiments were conducted at deformation temperatures of 293 K, 673 K, 873 K, 973 K, and 1073 K. The enhanced SHPB system is equipped with a synchronically assembled heating system. The setup of the enhanced SHPB system is schematically illustrated in Fig. 1. The system was used to ensure incident and transmit bars with a temperature below 523 K when the samples were heated to the desired uniform temperatures using a furnace independently. It can minimize the temperature gradient in the bars, preventing unwanted changes in the material parameters of the bars such as elastic constants and mechanical impedance [48, 49]. The synchronically assembled heating system was utilized to trigger the bar mover to make the two bars contact the sample. The system

achieved the instantaneous assembly of the bars and the sample right before the incident wave arrived at the interface between the incident bar and the sample.

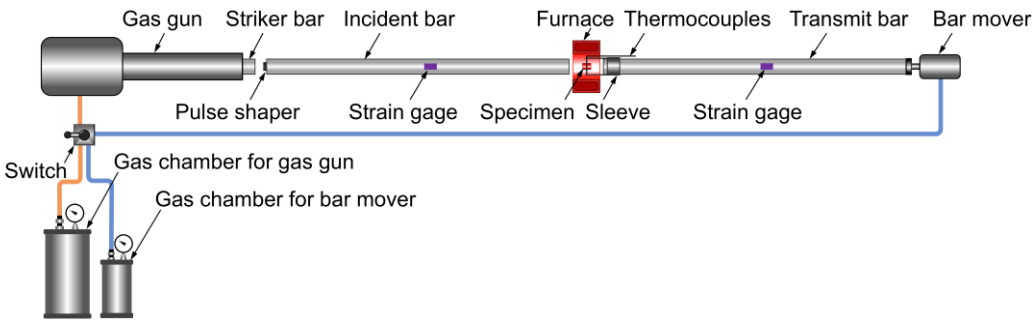

Fig. 1 Schematic drawing of the enhanced SHPB system

3. Experimental results

3.1 Initial microstructure

Figure 2A shows a EBSD inverse pole figure (IPF) map of the homogenized TiZrNbVTa RHEA, where the inset is the corresponding XRD pattern. The IPF map indicates the presence of randomly oriented equiaxed grains with an average grain size of approximately 340 μm. As illustrated in the XRD pattern, only one set of BCC diffraction peaks appears, revealing a single-phase BCC structure of the homogenized TiZrNbVTa RHEA. It can be further verified by the diffraction spots in the corresponding selected area electron diffraction (SAED) pattern of the TEM bright field image (Fig. 2C). The energy dispersive spectrometer (EDS) mapping images (Fig. 2B) confirm the elemental homogeneity at the nanoscale in the TiZrNbVTa RHEA.

Further crystallographic analysis for the homogenized TiZrNbVTa RHEA was conducted using the high-resolution transmission electron microscopy (HRTEM). Figure 2D shows the HRTEM image of the selected region in Fig. 2C, where severe lattice distortion appears. Figure 2E displays the inverse fast Fourier-transform (IFFT) image of the white box in Fig. 2D. The non-parallel lattice fringes marked by the yellow ellipse circles indicate severe lattice distortion of the RHEA. The presence of lattice

distortion was further confirmed by geometric phase analysis (GPA), which was using the (011) and $(0\bar{1}1)$ diffractions spots from Fig. 2C. The resulting atomic strain distribution maps along the ε_{xx}, ε_{xy}, and ε_{yy} directions are presented in Fig. 2F. The analysis revealed significant microscopic strain fluctuations induced by lattice distortion, which contribute to long-range lattice friction. This long-range lattice friction is accompanied by a decrease in the mobility of dislocations. Hence, the lattice distortion leads to an increase in the achievable yield strength of the solid-solution RHEAs [50]. The results highlight the critical role of lattice distortion in the strengthening mechanisms of the TiZrNbVTa RHEA.

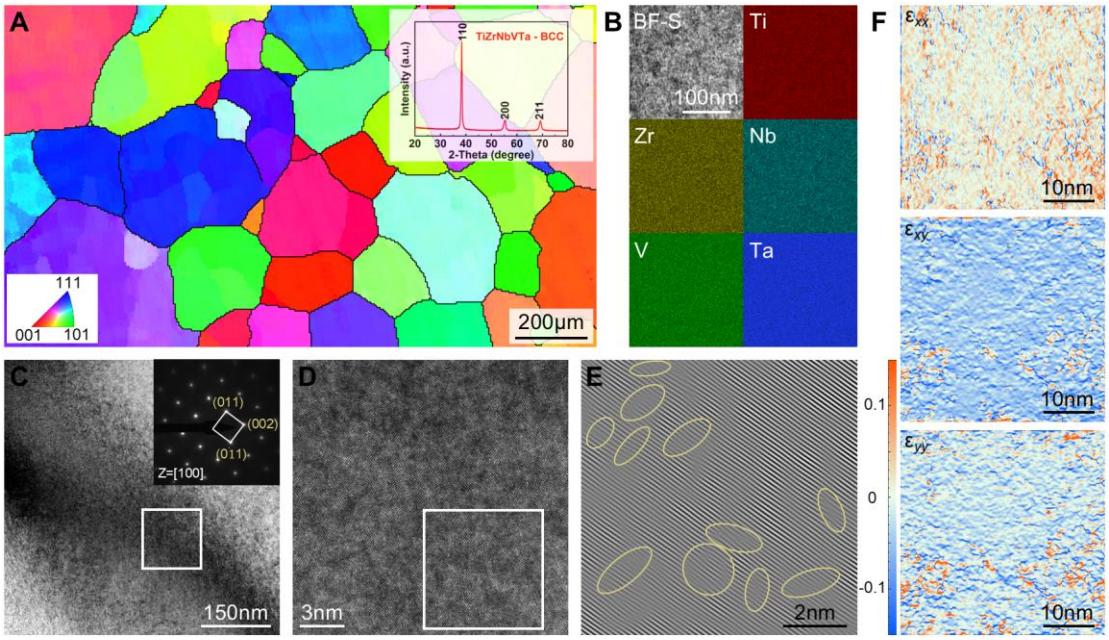

Fig. 2 Initial microstructure of the TiZrNbVTa RHEA: **A** IPF map, and the inset showing the corresponding XRD pattern; **B** EDS surface-scan distribution of five elements; **C** Bright field TEM image with the inset SAED pattern; **D** HRTEM image of the region marked by the white box in **C**; **E** IFFT pattern of the region marked by the white box in **D**, showing the lattice-fringe; **F** Atomic strain distribution maps of horizontal normal strain (ε_{xx}), shear strain (ε_{xy}), and vertical normal strain (ε_{yy}), determined by GPA from the region in **D**

3.2 Temperature and strain rate effects on the mechanical behavior

Figure 3 shows the true stress-strain curves of the TiZrNbVTa RHEA under compressive loadings over a wide range of temperatures (293 K – 1273 K) and strain rates (0.001 s^{-1} – 3000 s^{-1}). The RHEA exhibits ultrahigh yield strength and acceptable ductility over the selected temperature and strain rate range. As strain rate increases from 0.001 s^{-1} to 3000 s^{-1}, the yield strength of the TiZrNbVTa RHEA at a temperature of 293 K increases from about 1.3 GPa to about 1.7 GPa. The excellent yield strength under these conditions can be attributed to the influence of the severe lattice distortion [50]. The TiZrNbVTa RHEA exhibits apparent temperature sensitivity and remarkable high-temperature strength especially under high strain rates. For the quasi-static conditions, the temperature dependence of mechanical behavior can be characterized in three stages, as shown in Fig. 3A. The flow stress significantly increases with increasing plastic strain during the first stage (293 K – 473 K), showing significant strain hardening, but gradually decreases with increasing temperature, implying thermal softening. For the second stage (673 K – 873 K), serrated flow behaviors are observed, and the flow stress increases with increasing temperature, indicating an anomalous thermal hardening effect. Due to the recurrent pinning effect of solute atoms on dislocations during plastic deformation [51-53], the macroscopic phenomenon manifests as serrated flows on the stress-strain curves (as seen in the inset views in Fig. 3A), which is known as the Portevin-Le Chatelier dynamic strain aging (PLC DSA) [54, 55]. The characteristics of the serrations may vary with the applied strain rates or test temperatures [56-58], typically showing three types labeled as A, B, and C [57-59]. At 673 K, type B serrations fluctuate more rapidly around a general stress level, while at 873 K, type C serrations contain stress drops occurring below the general stress level. In the third stage (1073 K – 1273 K), continuous decrease of flow stress with increasing temperature is observed in Fig. 3A. Compared to the quasi-static condition, the RHEA shows significantly higher yield strength at dynamic conditions, while the fracture strain decreases. All samples, except for the one at 873 K, were compressed to fracture at a strain rate of 3000 s^{-1}. The yield strength of the RHEA remains above 800 MPa

even at 1073 K. Moreover, similar to the phenomenon observed under quasi-static condition, the flow stress at strain rates of 1000 s^{-1} and 3000 s^{-1} increases with temperature within a certain temperature range from about 873 K to 973 K, while the ductility significantly decreases at 973 K. This behavior deviates from the conventional understanding that flow stress typically decreases with increasing temperature, indicating an anomalous thermal hardening effect known as third-type strain aging (3rd SA) [60]. Previous studies [49, 61] have shown that the occurrence of the PLC DSA is accompanied by the 3rd SA, and both represent distinct manifestations of DSA.

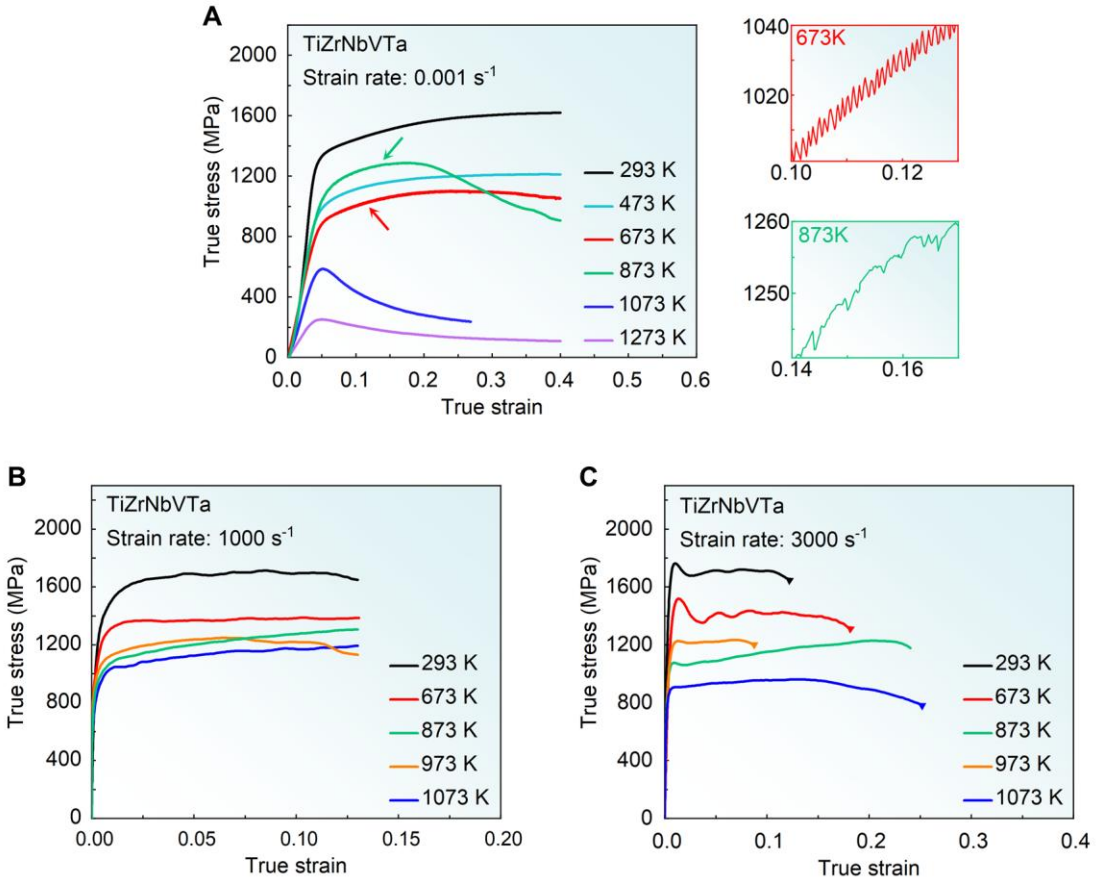

Fig. 3 True stress vs. true strain curves of the TiZrNbVTa RHEA at different strain rates: **A** 0.001 s^{-1}; **B** 1000 s^{-1}; **C** 3000 s^{-1}

To further understand the temperature effect on the flow stress at different strain rates, the flow stress vs. temperature relationship is plotted in Fig. 4. Under high strain rate loading, the heat generated by plastic deformation cannot dissipate rapidly into the

surroundings, resulting in a temperature rise within the sample. The actual instantaneous temperature of the sample can be calculated by the following expression [62, 63]:

$$T = T_0 + \Delta T = T_0 + \frac{\eta}{\rho C_V}\int_0^{\varepsilon} \sigma d\varepsilon \quad (1)$$

where T_0 is the initial test temperature, ΔT is the temperature rise, C_V represents the heat capacity (taken as 0.338 J/g K at room temperature), ρ is the density (taken as 8.48 g/cm^3), ε is the plastic strain, σ is the flow stress, and η is t he converted fraction of the heat generated by plastic work. Notably, setting η to 1 is appropriate for temperature rise calculations under high strain rate loading [49, 63-65]. In Fig. 4A, the flow stress initially decreases as the temperature rises from 293 K to 673 K, then increases to a peak at 873 K, followed by a sharp decrease. Figure 4B, C exhibits a consistent trend, and the peak occurs at approximately 910 K and 1010 K for strain rates of 1000 s^{-1} and 3000 s^{-1}, respectively. Figure 4D compares the flow stress vs. temperature curves at different strain rates. It can be observed that there is only a slight increase in flow stress from 1000 s^{-1} to 3000 s^{-1}, and even negative strain rate sensitivity appears above 873 K. Moreover, the anomalous stress peak shifts towards higher temperature regions as the strain rate increases.

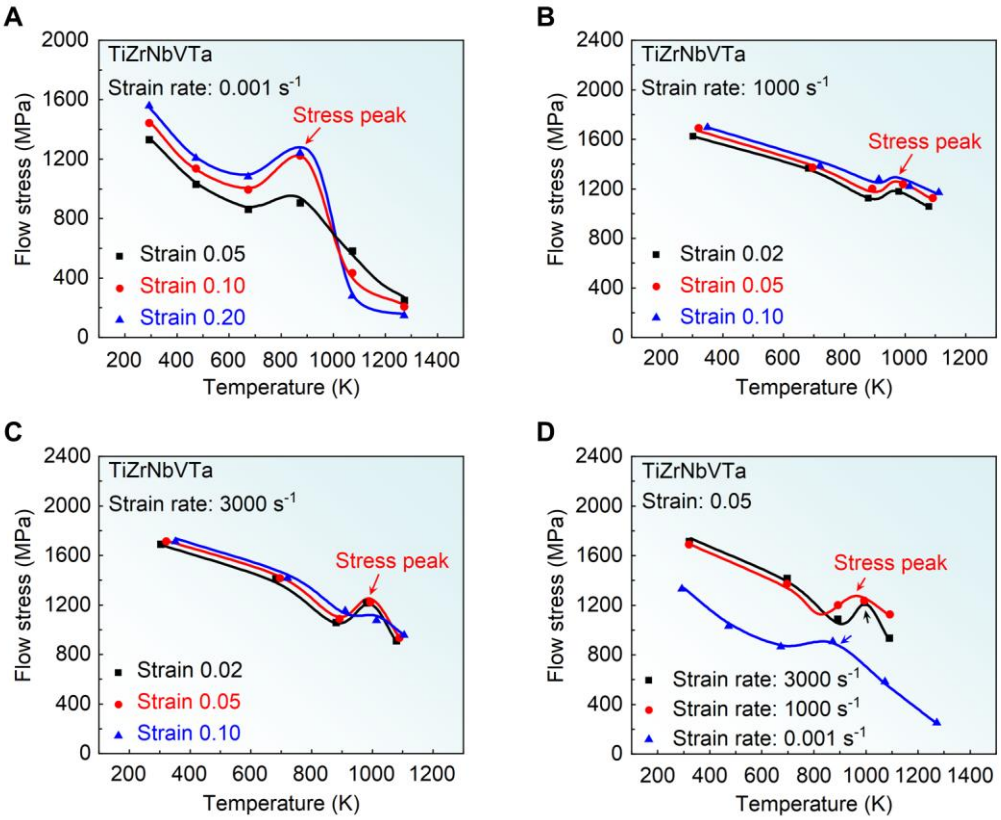

Fig. 4 Flow stress vs. temperature curves of the TiZrNbVTa RHEA at different strain rates: **A** 0.001 s^{-1}; **B** 1000 s^{-1}; **C** 3000 s^{-1}; **D** the variation of flow stress with temperature at different strain rates

3.3 Temperature and strain rate effects on microstructure evolution

To elucidate the deformation mechanisms and investigate the influence of temperature and strain rate on microstructure evolution, samples subjected to compression at different temperatures (293 K, 1073 K) and strain rates (0.001 s^{-1}, 3000 s^{-1}) were extracted from the mid-thickness section along the loading direction and subsequently characterized using EBSD and TEM techniques.

3.3.1 Temperature effect on microstructure evolution under quasi-static condition

Figure 5 shows the deformation microstructure of the TiZrNbVTa RHEA compressed at a temperature of 293 K and strain rate of 0.001 s^{-1}. The location of the EBSD observation region is illustrated in Fig. 5A. The IPF map in Fig. 5B shows that multiple grains exhibit pronounced deformation traces, e.g., multidirectional

orientation gradients marked by inconsistent color variations, as well as lamellar structures in some grains. These lamellar structures originate from grain boundaries and propagate within individual grains, exhibiting significant misorientations with respect to the matrix, similar to twinning bands or kink bands (KBs) observed in deformed alloys [66, 67]. The grain boundaries (GBs) map (Fig. 5C) and Kernel average misorientation (KAM) map (Fig. 5D) clearly highlight the presence of the rather unusual lamellar structures. These observations indicate that most of the geometrically necessary dislocations (GNDs) are confined close to the grain boundaries.

Figure 5E shows an enlarged IPF map of the smaller dashed box in Fig. 5B. The misorientation profile along line 1 in Fig. 5F shows that the lamellar structures and matrix exhibit arbitrary misorientations in the range of 40° – 50°, which is far from the constant misorientation of twinning in BCC alloys (50.5° for {332} <113> twin and 60° for {112} <111> twin) [68], thereby excluding the possibility of twinning. Therefore, these bands can be reasonably identified as KBs. For BCC alloys, kinking is another common deformation mechanism apart from dislocation activity [69]. The intergranular misorientation axis (IGMA) analysis based on dislocation slip-induced lattice rotation, is widely used to confirm the existence of KBs [70, 71]. The lattice rotation axis (T) during kinking can be expressed as $T = \gamma b \times n$, where γ, b, and n respectively represent the plastic shear gradient, the Burgers vector, and the slip plane normal vector of the slip system [72]. In BCC alloys, the Burgers vector b of the perfect slip dislocation is of the type 1/2<111>, while the slip planes n have three types, i.e., {110}, {112}, and {123}. The corresponding rotation axes T can be deduced as <112>, <011>, and <541>. Therefore, the invariant crystal plane of the KB is one of {112}, {011}, or {541} during deformation. Detailed explanations will be provided in a later section. Figure 5G lists the {112}, {011}, and {541} pole figures of the white dashed box in Fig. 5E. The {011} pole figure shows a distinct pole focus, and the remaining poles in the {011}, {112}, and {541} pole figures rotate around this pole focus. This crystallography confirms the presence of KBs in Fig. 5E, where the lattice rotation axis

of <011> corresponds to the activation of the <111> {112} slip mode during the kinking process.

For kinking behavior in BCC alloys, it has been proposed that the formation of KBs progresses through three stages: the dislocation gliding stage, the pre-kinking stage, and the ripening of pre-KBs stage [73, 74]. Pre-KBs, characterized as low-angle grain boundaries (LAGBs) with misorientation below 15°, gradually develop into mature KBs through continuous dislocation activity. In the enlarged IPF map shown in Fig. 5H, two KBs with different orientations are observed within a single grain. These boundaries exhibit misorientations ranging from 13° to 25° relative to the matrix, as presented in Fig. 5I, K. Based on these features, the two KBs are inferred to correspond to the ripening of pre-KBs stage [73]. Figure 5J, L illustrates that one pole focuses on {011}, and another pole focuses on {112}, while the remaining poles rotate around the <011> or <112> poles. This indicates the activation of the <111> {112} and <111> {110} slip systems, respectively. TEM analysis was performed to gain deeper insights into the deformation mechanisms in TiZrNbVTa RHEA, with a particular focus on the formation of KBs. The corresponding images are presented in Fig. 5M–O. The density of dislocations is found to be accumulated and rearranged to form dislocation walls in localized zones, as shown in Fig. 5M. For the zone of dislocation walls (Fig. 5N), the diffraction spots exhibit diffraction arcs extending up to approximately 20° (Fig. $5N_1$). This indicates that orientational rotation of dislocation walls has taken place, which defines the kink zone [73]. The rotated dislocation walls are just confined to the interiors of kink zone, while the adjacent matrix is still characterized by high dislocation density and coarse grain. These observations suggest that the presence of the dislocation wall is a prerequisite for kinking. The HRTEM image and the inset IFFT (Fig. $5O_1$) reveal the presence of numerous dislocations, and the formation of dislocation pairs with opposite signs , as observed in the inset, contributes to the nucleation of KBs [75].

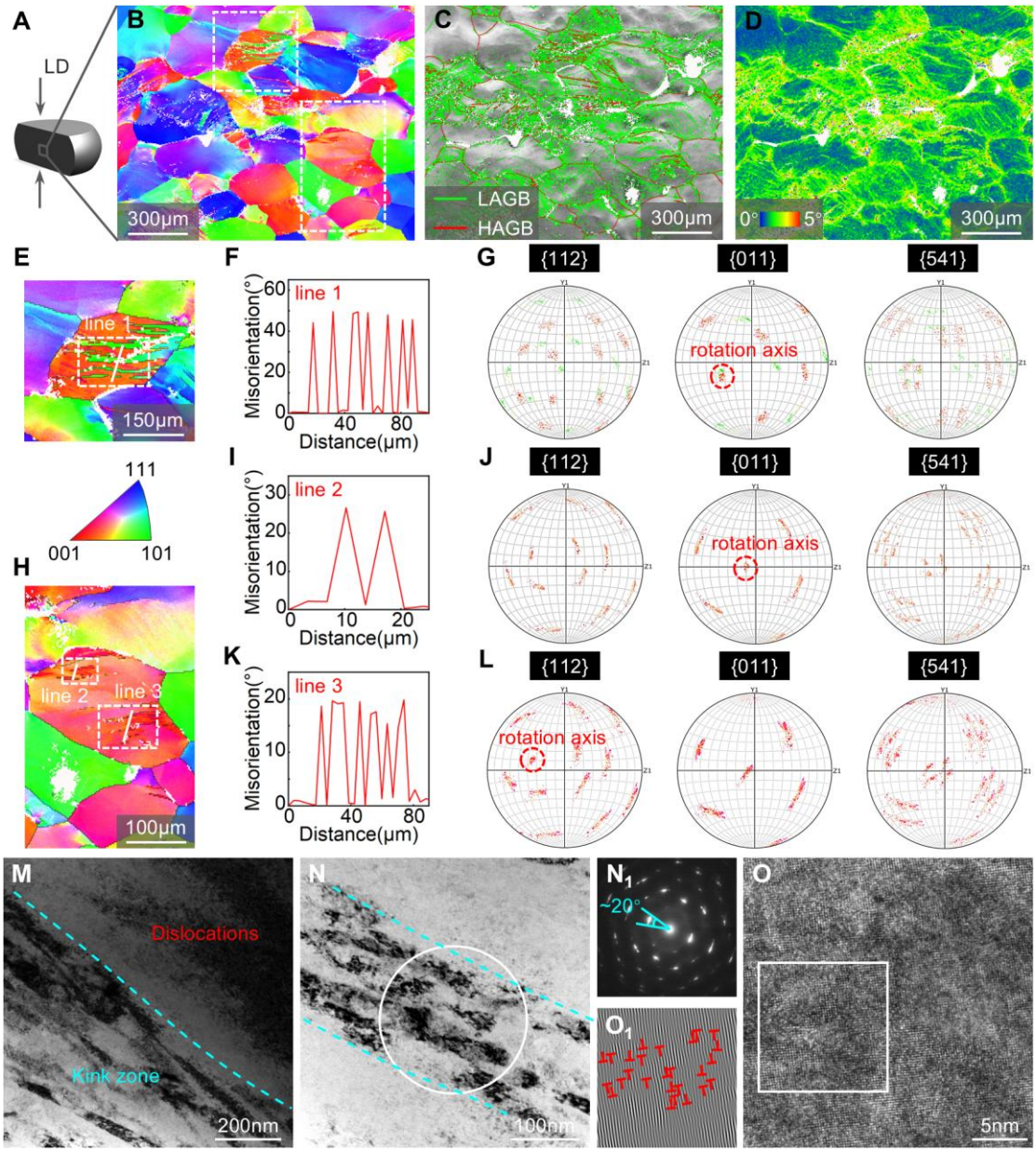

Fig. 5 Microstructure of the TiZrNbVTa RHEA compressed at 293 K and strain rate of 0.001 s^{-1}: **A** Schematic illustration of the observed region; **B-D** EBSD maps; **E**, **H** Enlarged IPF maps; **F**, **I**, **K** Misorientation profiles along line 1, 2, 3, respectively; **G** Pole figures of the region marked in **E**; **J** Pole figures of the region marked by the smaller box in **H**; **L** Pole figures of the region marked by the larger box in **H**; **M**, **N** Bright field TEM images; $\mathbf{N_1}$ The SAED pattern obtained from **N**; **O** HRTEM image, and the corresponding IFFT image shown in $\mathbf{O_1}$ (red '⊥' denotes dislocations in $\mathbf{O_1}$)

Figure 6 presents the deformation microstructure of the TiZrNbVTa RHEA compressed at a temperature of 1073 K and strain rate of 0.001 s^{-1}. The location of the EBSD observation region is consistent with that in Fig. 5A. Figure 6A shows the EBSD

IPF map of the deformed sample. A shear localization region is observed along a direction inclined at an angle to the loading direction. Some fine dynamic recrystallization (DRX) grains with distinct misorientation are observed. In the GB maps (Fig. 6B), a large number of LAGBs are observed in the shear localization region. The KAM map in Fig. 6C shows a high density of GNDs within the shear localization region, indicating that severe deformation occurs in this region. Due to the limited resolution of the EBSD detector, only larger grains can be detected, while some nanoscale DRX grains remain undetected. TEM was used to characterize the central region of the shear band to further reveal its microstructure evolution, as shown in Fig. 6D–F. Figure 6D shows numerous nanoscale grains, while the inset SAED pattern displays a complex multi-spot arrangement, indicating the presence of multiple sub-grains with varying orientations in the region. The elongation of the diffraction spots is attributed to lattice misorientation within the heavily deformed grain. Figure 6E shows the nucleation process of DRX, with a high density of dislocations in the upper-left corner and recrystallized grains in the lower-right corner. The nucleation of sub-grains and the trapping of mobile dislocations at the sub-grain boundaries (Fig. 6F) lead to increased misorientation, suggesting that continuous dynamic recrystallization (CDRX) may act as the nucleation mechanism for recrystallization [76]. CDRX is considered a recovery process, progressing through the continual absorption of dislocations at sub-grain boundaries, ultimately leading to the formation of new grains [77]. Some recrystallized grains contain numerous dislocations, suggesting that these grains may underwent further deformation under severe shear stress. Moreover, it is worth noting that KBs are absent under the current deformation conditions, underscoring the need to consider the influence of deformation temperature. Detailed discussion will be provided in a later section.

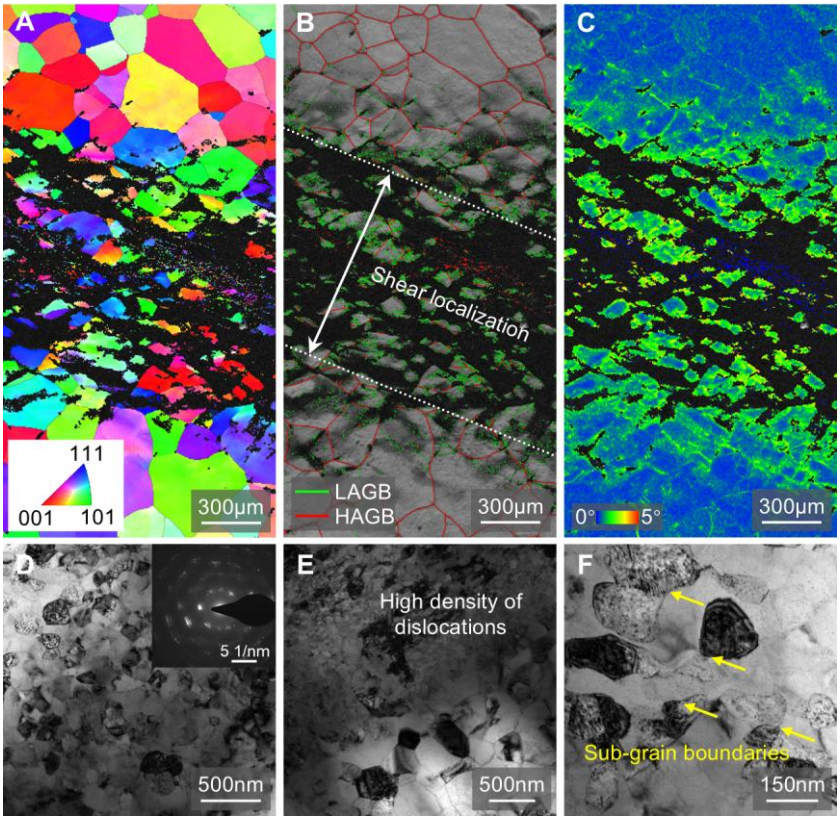

Fig. 6 Deformation microstructure of the TiZrNbVTa RHEA compressed at a temperature of 1073 K and strain rate of 0.001 s^{-1}: **A** IPF map; **B** GBs map; **C** KAM map; **D** Bright field TEM image, showing fine sub-grains in the core of shear localization and the corresponding SAED pattern; **E** Bright field TEM image, showing high-density dislocation activity and the formation of DRX grains; **F** Bright field TEM image, indicating the sub-grain boundaries

3.3.2 Temperature effect on microstructure evolution at high strain rate

Considering the strain rate effect on the mechanical behavior of the TiZrNbVTa RHEA, EBSD and TEM observations were also conducted on the samples deformed at a high strain rate (3000 s^{-1}) and different temperatures (293 K and 1073 K). Figure 7 presents the deformation microstructure of the TiZrNbVTa RHEA compressed at a temperature of 293 K and strain rate of 3000 s^{-1}. Figure 7A schematically illustrates that the sample fractured along a plane oriented at an angle to the loading direction, and the gray rectangular area was selected as the region for EBSD observation and subsequent TEM observation. A large number of lamellar KBs are observed within grains, as presented in Fig. 7B. Combining with the corresponding GB map in Fig. 7C,

it can be observed that the crack propagates through the grains, and the fracture mode of the sample belongs to transgranular fracture. The GNDs in the KAM map shown in Fig. 7D are predominantly concentrated at the boundaries of KBs and grain boundary near the fracture surface. Figure 7E shows an enlarged IPF map of the black dashed box in Fig. 7B. The variation of misorientation profile determined along the black line in Fig. 7E is displayed in Fig. 7F, implying that the misorientation of adjacent KBs falls within the range from about 25° to 30°. The pole figures shown in Fig. 7G, corresponding to the region of Fig. 7E, exhibit strong misorientation around both {011} and {541} poles, further confirming the formation of KBs.

Figure 7H–J shows the bright field TEM images, revealing pronounced dislocation activity. As shown in Fig. 7H, dislocations multiply rapidly and predominantly glide on the $\{10\bar{1}\}$ plane, resulting in dislocation walls with high dislocation density. The inset SAED pattern shows diffraction spots with brilliant contrast, indicating the absence of misorientation. Based on the preceding analysis, the formation of such dislocation walls may set the conditions for the appearance of KBs, corresponding to the dislocation gliding stage. As shown in Fig. 7I, slip bands from different traces intersect, and dislocation dipolar walls intersect to form an extensively networked dislocation pattern. The magnified dislocation morphology of the white box in Fig. 7I reveals dipoles composed of dislocations with opposite Burgers vectors, as shown in Fig. 7J, which contributes to the nucleation of KBs [75].

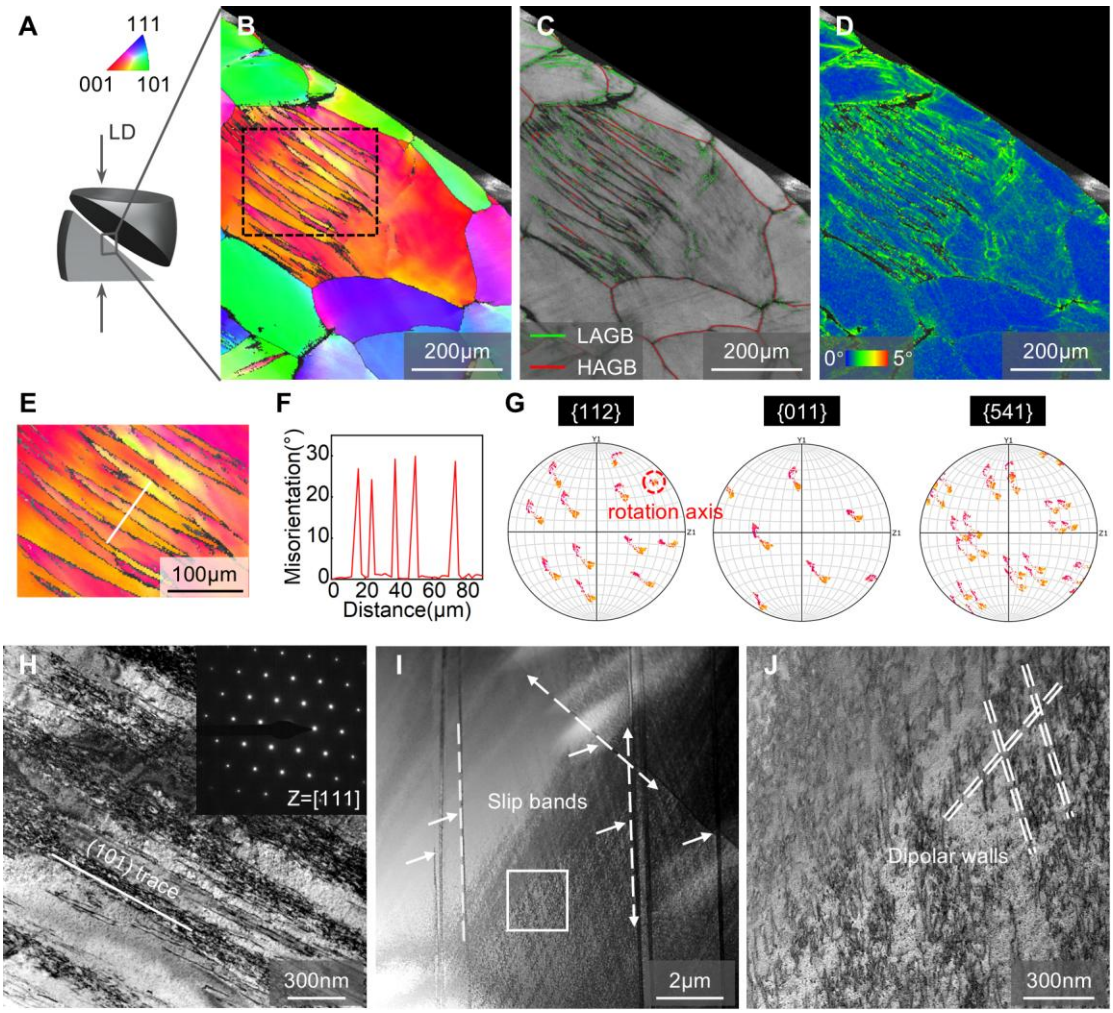

Fig. 7 Deformation microstructure of the TiZrNbVTa RHEA compressed at a temperature of 293 K and strain rate of 3000 s^{-1}: **A** Schematic illustration of the regions for microstructure observation; **B** IPF map; **C** GBs map; **D** KAM map; **E** The enlarged view of the region marked by the black box in **B**; **F** Misorientation profile along the white line insert in **E**; **G** {112} {011}, and {541} pole figures of **E**; **H** Bright field TEM image, displaying the dislocation walls and the corresponding SAED pattern; **I** Bright-field TEM image, showing interacting slip bands and the network of dipolar walls; **J** High magnification image of the region marked by the white box in **I**

Figure 8 shows TEM images of the TiZrNbVTa RHEA compressed at a temperature of 293 K and strain rate of 3000 s^{-1}, indicating a stress-induced martensitic transformation (SIMT) from BCC to omega (ω) phase. Due to the low volume fraction and significantly smaller size compared to the BCC phase, the ω phase cannot be clearly identified in the EBSD map. Figure 8A shows a TEM micrograph and a SAED pattern of the white-circled area, indicating the formation of the ω phase. The ω structure is a

non-close-packed hexagonal crystal with the space group of P6/mmm. The ω phase exhibits a characteristic of lamellar morphology with individual layer thicknesses of approximately 100 nm, which is attributed to a displacive shear transformation mechanism to reduce the strain energy, as described by Eshelby's inclusion theory [78]. As shown in the EDS element maps in Fig. 8B, the ω phase exhibits no elemental segregation, further supporting the stress-induced transformation. The HRTEM image in Fig. 8C displays the interface between BCC matrix and ω phase. The BCC matrix and ω phase are respectively verified by the Fast Fourier Transform (FFT) results shown in the insets of Fig. 8C. The ω phase (left) and the BCC matrix (right) are separated by the phase boundary (blue dashed line). Figure 8D presents the atomic strain distribution map, suggesting that the ω phase impedes dislocation motion in the BCC matrix and thereby intensifying its lattice distortion. Figure 8E shows the IFFT result corresponding to the region marked by the white box in Fig. 8C, revealing that the dislocations within the ω phase imply the excellent deformability of the stress-induced lamellar ω phase. Additionally, Fig. 8F shows that the interphase boundary effectively impedes dislocation slip, resulting in dislocation pile-ups (indicated by red arrows) at the interphase boundaries. The deformability of the lamellar ω phase and the dislocations pile-up can further enhance the combination of strength and ductility of the RHEA.

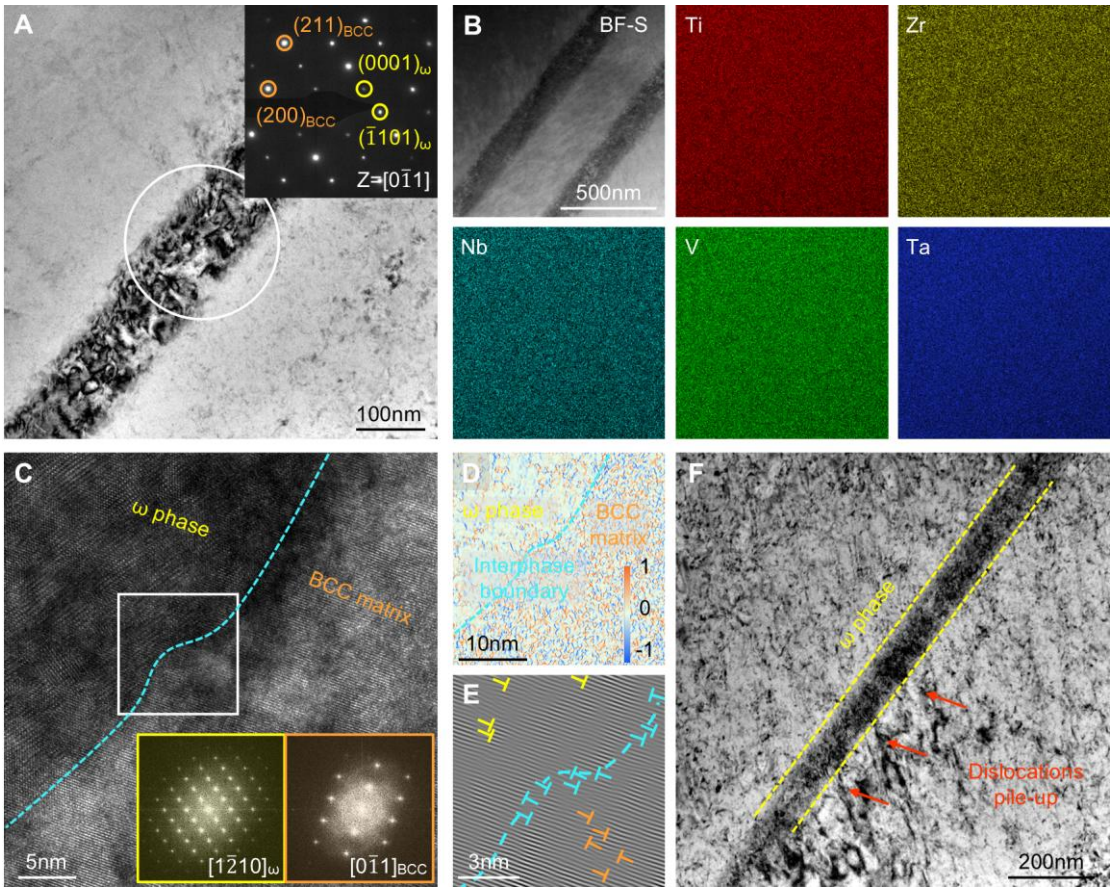

Fig. 8 TEM images revealing the stress-induced martensite transformation in the TiZrNbVTa RHEA compressed at a temperature of 293 K and strain rate of 3000 s^{-1}: **A** Bright field TEM image and SAED pattern, showing both the BCC phase and the lamellar ω phase; **B** Bright field STEM image and EDS element maps of the ω phase, indicating no elemental segregation; **C** The HRTEM image, showing the interface between the BCC and ω phases, and the insets displaying the FFT pattern of both phases; **D** Atomic strain distribution map of horizontal normal strain (ε_{xx}), determined by GPA from the region in **C**; **E** The IFFT pattern of the region marked by the white box in **C**, with dislocations marked by colored '⊥' symbols: yellow for those within the ω phase, orange within the BCC matrix, and cyan located at the phase boundary; **F** Bright field TEM image, showing dislocation pile-ups at the interphase boundary

Figure 9 presents the deformation microstructure of the TiZrNbVTa RHEA compressed at a temperature of 1073 K and strain rate of 3000 s^{-1}. The location of the EBSD observation region is consistent with that in Fig. 7A. As shown in Fig. 9A, an array of KBs is aligned parallel to each other in the upper portion. The observed KBs predominantly originates at the GBs and subsequently spreads into the grains. Moreover,

secondary KBs appear adjacent to the parallel KB arrays. Small-sized KBs characterized by LAGBs and a high density of GNDs are observed in the lower portion, as shown in Fig. 9B, C. Figure 9D, H provides enlarged views of the white boxes in Fig. 9A. As shown in Fig. 9E, the misorientation profile along line 1 in Fig. 9D reveal that the misorientation of the parallel KB array varies between 37° to 43°. In contrast, the misorientation profiles along line 2 and line 3, as displayed in Fig. 9F, I, reveal misorientations below 15°. The pole figures corresponding to the regions of Fig. 9D, H are respectively displayed in Fig. 9G, J, displaying distinct poles focus in {011} and {112} planes. These observations confirm the presence of pre-KBs. It has been proposed that KBs form through the growth and coalescence of multiple pre-KBs [73]. These findings contribute to understanding the propagation behavior of KBs.

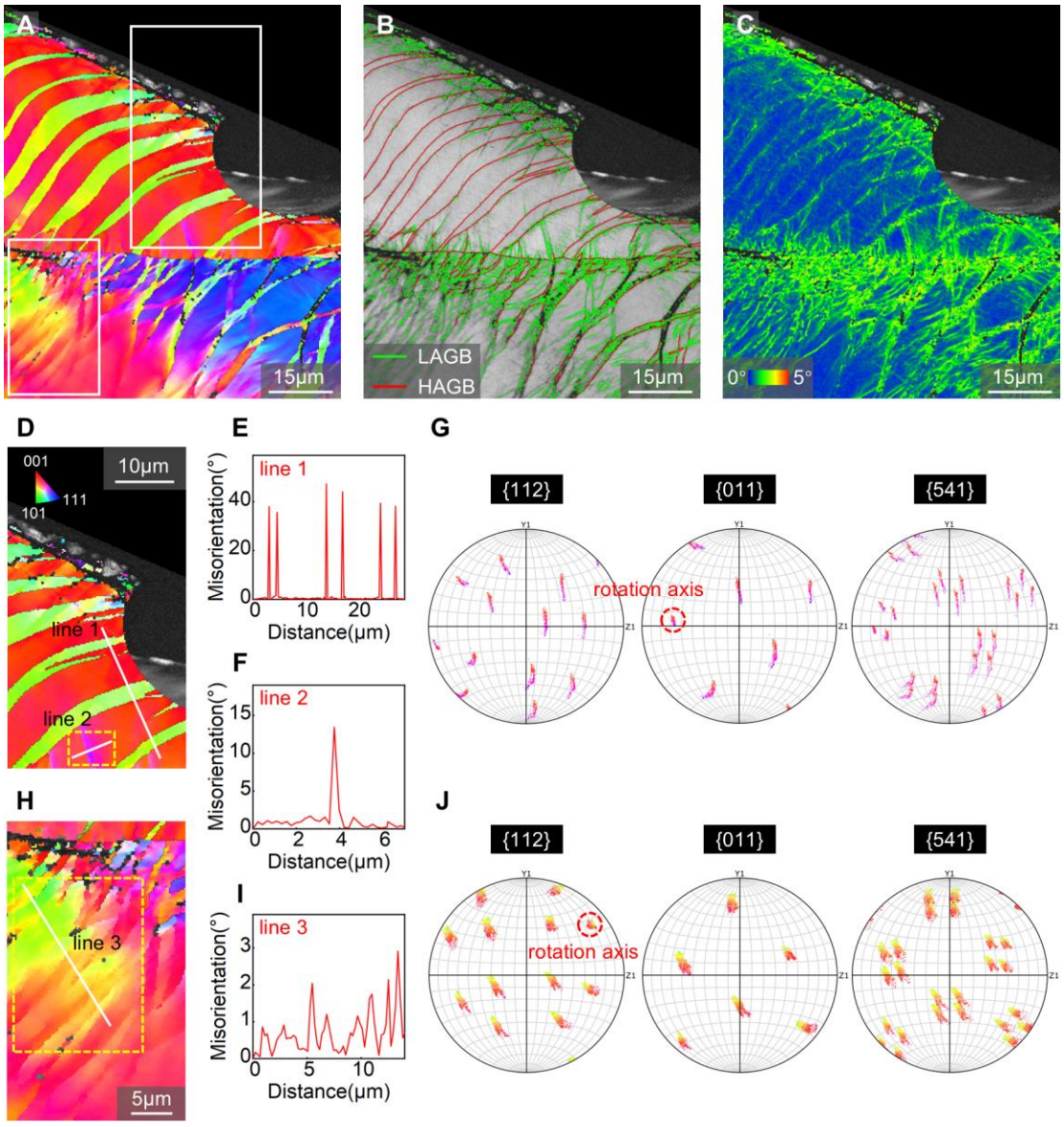

Fig. 9 Deformation microstructure of the TiZrNbVTa RHEA compressed at a temperature of 1073 K and strain rate of 3000 s^{-1}: **A** IPF map; **B** GBs map; **C** KAM map; **D** The enlarged view of the region marked by the larger box in **A**; **E** Misorientation profile along the line 1 insert in **D**; **F** Misorientation profile along the line 2 insert in **D**; **G** {112}, {011}, and {541} pole figures of the region marked by the yellow box in **D**; **H** The enlarged view of the region marked by the smaller box in **A**; **I** Misorientation profile along line 3 insert in **H**; **J** {112}, {011}, and {541} pole figures of the region marked by the yellow box in **H**

Figure 10 shows TEM images of the TiZrNbVTa RHEA compressed at a temperature of 1073 K and strain rate of 3000 s^{-1}, indicating a SIMT from BCC to ω phase. This transformation is consistent with that observed at 293 K under the same

strain rate. Figure 10A presents a TEM micrograph and a SAED pattern indexed from the [113] BCC zone axis, confirming the presence of the ω phase. Notably, the martensitic lath spacing is finer than that of the sample deformed at 293 K. The EDS map in Fig. 10B shows no apparent elemental segregation at the phase boundaries. HRTEM images of the interface between BCC matrix and ω phase are shown in Fig. 10C. The insets in Fig. 10C present the FFT results from both sides of the interphase, confirming the presence of both the BCC matrix and the ω phase. Additionally, the atomic strain distribution shown in Fig. 10D indicates that the ω phase acts as a barrier to dislocation motion within the BCC matrix, thereby intensifying its lattice distortion. During phase transformation, the deformation gradient at the interfaces is accommodated by the generation of necessary dislocations, as shown in Fig. 10E. As shown in Fig. 10F, dislocation slip is hindered by phase boundaries, leading to dislocation pile-ups and thereby contributing to the strain hardening capacity of the TiZrNbVTa RHEA [79]. Furthermore, compared to the sample deformed at 293 K (Fig. 8), the sample deformed at a high temperature (1073 K) exhibits a denser and more homogeneous dislocation distribution within both the matrix and the ω phase.

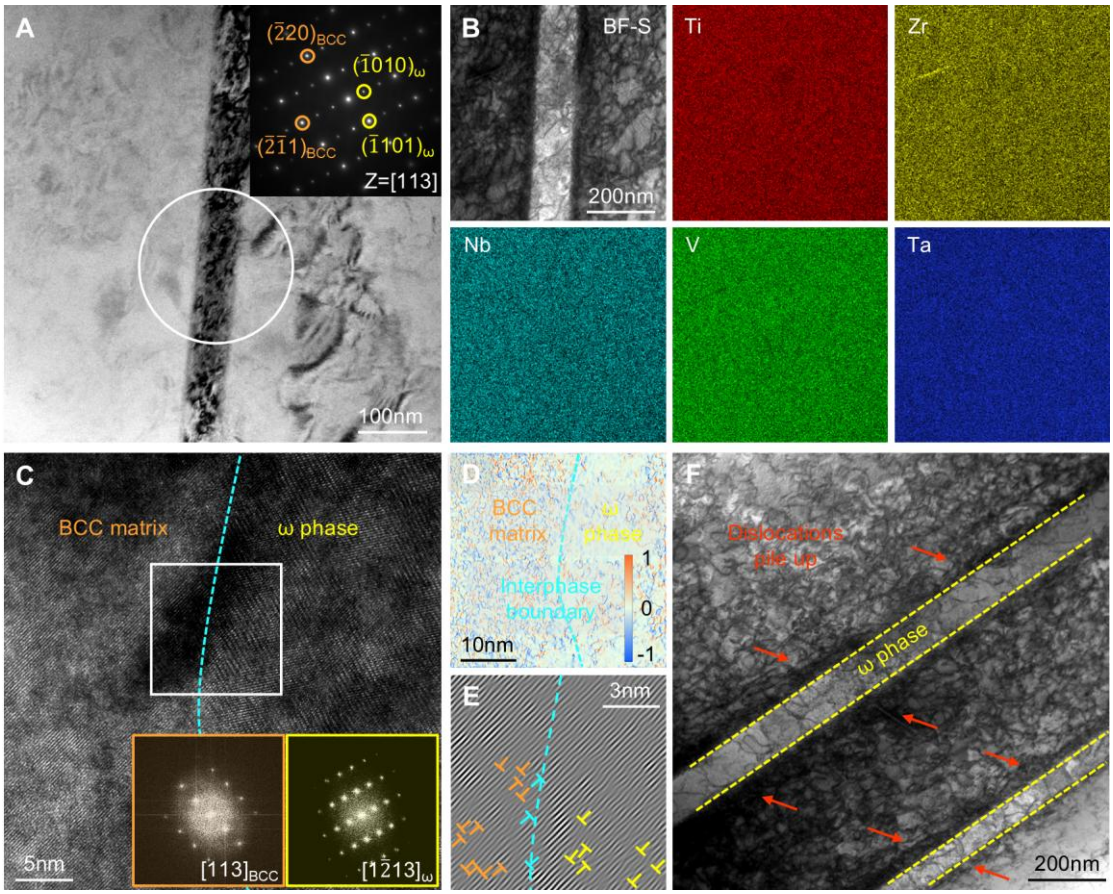

Fig. 10 TEM images revealing the martensitic microstructure in the TiZrNbVTa RHEA compressed at a temperature of 1073 K and strain rate of 3000 s^{-1}: **A** Bright field TEM image and SAED pattern, showing both the BCC phase and the ω phase; **B** Bright field STEM image and EDS element maps of the martensite structure, indicating the absence of elemental segregation; **C** The HRTEM image, showing the interface between the BCC and ω phases, with insets displaying the FFT patterns of both phases; **D** Atomic strain distribution map of horizontal normal strain (ε_{xx}), determined by GPA from the region in **C**; **E** The IFFT pattern of the region marked by the white box in **C**, with dislocations marked by colored '⊥' symbols: yellow for those within the ω phase, orange within the BCC matrix, and cyan located at the phase boundary; **F** Bright field TEM image, showing dislocation pile-ups at the interphase boundary

4. Discussion

As described above, the TiZrNbVTa RHEA exhibits an exceptional combination of strength and ductility over a wide range of temperatures and strain rates. The severe

lattice distortion of the single-phase BCC solid solution, along with the 3rd SA effect, contributes to the high yield strength of the homogenized TiZrNbVTa RHEA over the selected temperature range. To elucidate the origins of the remarkable mechanical properties, the microstructure evolution of the deformed RHEA was investigated. KBs and SIMT were observed in the deformed samples across different deformation temperatures and strain rates, which play key roles in achieving superior strength and ductility. Their formation mechanisms and strengthening contributions will be discussed in detail in the following sections.

4.1 Strengthening mechanism of severe lattice distortion

As shown in Fig. 1, the single-phase BCC structure, uniform grain distribution, and a homogenized atomic distribution of the TiZrNbVTa RHEA were achieved after heat treatments. The RHEA demonstrates severe lattice distortion and significant microscopic strain fluctuations. Severe lattice distortion, one of the four core effects in single-phase HEA, plays a vital role in enhancing yield strength. These distortions originate from the random distribution of constituent elements with appreciable size variations.

Solid-solution strengthening, primarily driven by lattice distortion effect, is a key mechanism contributing to the mechanical performance of the TiZrNbVTa RHEA. Despite its simple microstructure, the equimolar composition of multi-principal elements in the RHEA facilitates a unique solid-solution strengthening effect, significantly improving its mechanical properties. The enhancement of the solid-solution strengthening due to lattice distortion is closely associated with variations in atomic sizes and bond lengths within the RHEA, which arise from chemical interactions among the constituent multi-principal elements. Specifically, the homogeneous distribution of solute atoms in the TiZrNbVTa RHEA induces significant lattice distortion, which generates long-range lattice friction that effectively hinders dislocation mobility. Moreover, it has been proposed that the addition of an equiatomic percentage of the Zr element promotes the effect of solid-solution strengthening in the

NbTaTiV RHEA [50]. This enhancement leads to an increase of about 300 MPa in yield strength of the RHEA. Zr, with its larger atomic radius compared to the other constituent elements, expands the range of bond lengths for nearly all atomic-species pairs in the NbTaTiVZr system. In conclusion, severe lattice distortion plays a crucial role in optimizing the yield strength of the TiZrNbVTa RHEA. This study highlights the potential of lattice distortion as a key design strategy for improving the strength of RHEAs.

4.2 3rd SA effect on the combination of strength and ductility

As shown in Figs. 3, 4, the flow stress level increases with temperature within a certain range, forming an anomalous stress peak in the flow stress versus temperature relation. Beyond this range, the flow stress decreases sharply again with increasing temperature. Consequently, a bell-shaped peak appears in the stress vs. temperature curve, which is identified as the 3rd SA. This behavior contrasts with the conventional understanding that the flow stress of metallic materials typically decreases with increasing temperature. Furthermore, as the strain rate increases, the anomalous stress peak shifts to a higher temperature range, while its amplitude decreases, as displayed in Fig. 4D. It is generally accepted that the 3rd SA is related to the dynamic pinning effect on moving dislocations by diffusing solute atoms while dislocations are “waiting” at their short-range barriers [80]. The formation of solute atom atmospheres includes: (1) the Cottrell atmosphere [81] (solute segregation around dislocation cores), (2) the Sneok atmosphere [82, 83] (dislocation stress-field induced short-range ordering (SRO)), and (3) the Suzuki atmosphere [84, 85] (solute segregation on stacking faults in extended dislocations). It is worth mentioning that for the 3rd SA to occur, a certain level of plastic deformation is necessary and the interaction between the solute atoms and the dislocations increases with plastic deformation.

During plastic deformation, temperature affects the migration of atoms and vacancies and further the position adjustment, while strain rates influence the number and mobility of dislocations nucleated in the alloy under stress. When the temperature

and strain rate reach a specific relationship, atom atmospheres or short-range clusters (SRCs) form around mobile dislocations, effectively pinning them. This relationship between temperature and strain rate can be expressed as follows [49, 86, 87]:

$$\dot{\varepsilon} = \frac{4b\rho D}{l} = \frac{4b\rho C_v D_0 exp(-Q_m/RT)}{l} \quad (2)$$

where b is the Burgers vector, l is the effective radius of the solute atom atmosphere, D is the diffusion coefficient of solute atoms, D_0 is the diffusion frequency factor, ρ is the mobile dislocation density, Q_m is the effective activation energy associated with the stress peak induced by the 3rd SA, C_v is the vacancy density, and R is the universal gas constant. As plastic deformation progresses, both ρ and C_v evolve with increasing plastic strain. They can be correlated with plastic strain, ε, i.e., $C_v \propto \varepsilon^{\alpha}$, and $\rho \propto \varepsilon^{\beta}$, where α and β are material constants. When the coupling effects of the temperature and strain rate approach a critical combination, the solute atom atmosphere attains its maximum capacity to pin the mobile dislocations and the flow stress achieves its peak value. As the temperature increases further, the diffusion velocity of the solute atoms (v_{diff}) surpasses the corresponding velocity of the mobile dislocation (v_{dis}), leading to a weakened pinning effect. At low temperatures and high strain rates, v_{diff} is lower than v_{dis}, and as a result, the 3rd SA does not occur. Consequently, as the strain rate increases, the anomalous stress peak shifts to a higher temperature range, and its amplitude decreases.

For RHEAs, there is confusion to researchers about which atoms act as "solutes" to form atmospheres around mobile dislocations. Unlike conventional alloys, RHEAs lack distinct "solvents" or "solutes" atoms as defined by the traditional notions of solid solution hardening. Despite this, the 3rd SA and PLC DSA have been observed in the TiZrNbVTa RHEA in this work. The equiatomic composition of multiple elements in the TiZrNbVTa RHEA favor the formation of local atomic environments [88], such as segregation or chemical ordering. These unique environments may pin dislocations on the slip plane, increasing the flow stress needed for dislocation escape and thereby contributing to the occurrence of a 3rd SA effect. A critical question arises: which atoms act as "solutes" to form solute atom atmospheres around mobile dislocations? Figure

11 displays TEM images of the deformed sample at a strain rate of 0.001 s^{-1} and temperature of 873 K, close to the peak temperature of the 3rd SA. A large number of KBs were also observed under the same condition in the corresponding EBSD analysis, as shown in Fig. S1. Figure 11A presents a TEM image along with its corresponding SAED pattern, which reveals streak-like features along the [100] principal crystallographic axis. Further microstructural details are visible in the high-magnification bright field STEM image provided in Fig. 11C. The contrast features observed in this image, together with the SAED pattern (inset in Fig. 11A) suggest the presence of local chemical or structural ordering. Figure 11B presents an HRTEM image and the corresponding FFT pattern. The FFT pattern shows streak-like features extending from the main diffraction spots toward shorter reciprocal vectors, consistent with the SAED pattern in Fig. 11A. The EDS element maps in Fig. 11D reveal pronounced Zr segregation within the local structure, accompanied by the depletion of other constituent elements. These observations imply the existence of Zr-enriched SRCs. Such local enrichment leads to bending of the lattice layers at the SRC, as observed in the HRTEM image (Fig. 11B), which can be attributed to the clustering of larger Zr atoms [89]. Based on these findings, Zr atoms are likely to function as "solutes". It is well known that the stress field in lattice created by dislocations is the driving force for the relative position adjustment of adjacent atoms to reduce the overall strain energy. Oversized atoms tend to segregate in the dilated part of edge dislocations to decrease the lattice strain around dislocation, while undersized atoms preferentially migrate to the compressed region [90]. This stress-induced atomic migration leads to the formation of Zr-enriched SRCs, thereby effectively pinning the dislocations. Figure $11B_1$ shows the IFFT result of the region marked by the blue box in Fig. 11B, indicating that dislocations are blocked by the SRCs. Additionally, Fig. $11B_2$ illustrates the atomic strain distribution map, highlighting localized strain around the SRCs due to dislocation blockage. Consequently, a higher stress is required to overcome the pinning and facilitate dislocation motion. This results in a 3rd SA effect, manifesting as an

anomalous stress peak in the flow stress vs. temperature curve over the temperature range of 3rd SA.

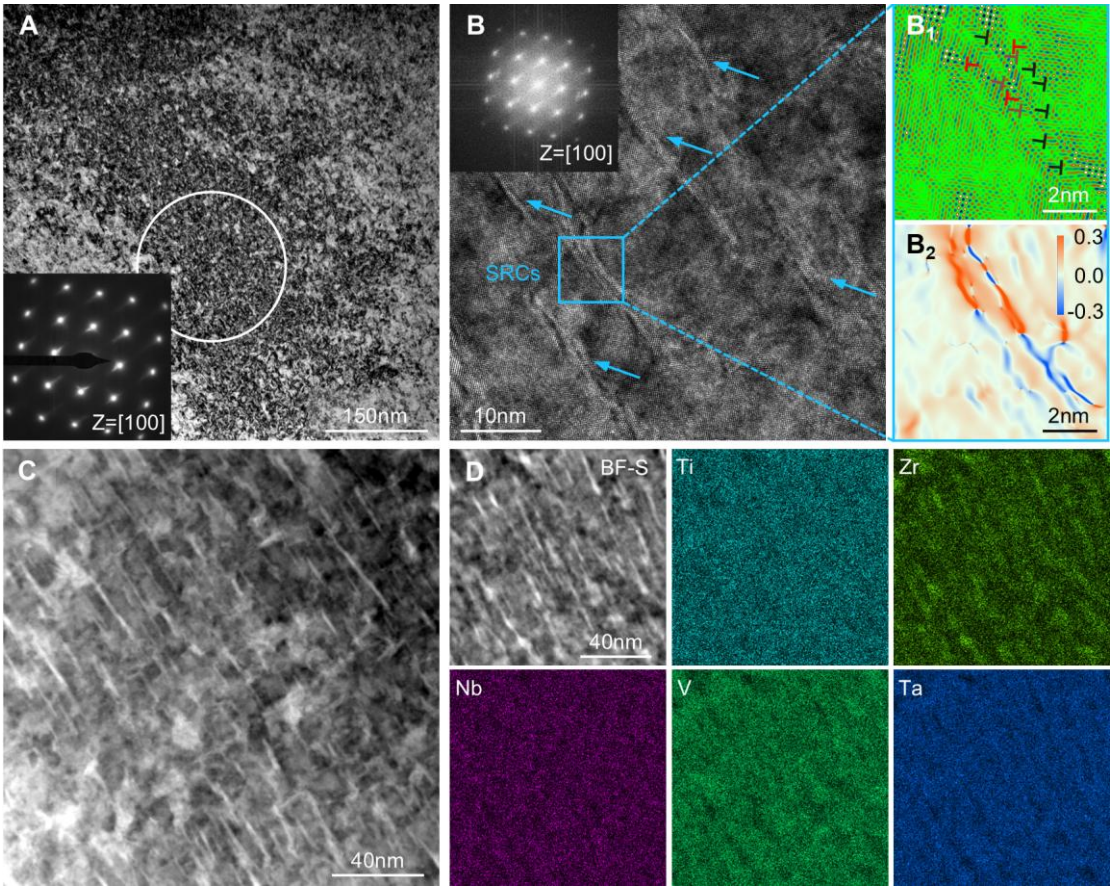

Fig. 11 Deformation microstructure of the TiZrNbVTa RHEA compressed at a temperature of 873 K and strain rate of 0.001 s^{-1}, corresponding to the peak of the 3rd SA: **A** Bright field TEM image and SAED pattern, showing abundant dislocations and SRCs; **B** HRTEM image obtained from the interior of the white-circled area in **A**, along with its corresponding FFT, revealing the presence of SRCs; **B_1** IFFT pattern of the region marked by the blue box in **B**; **B_2** Atomic strain distribution map of horizontal normal strain (ε_{xx}), determined by GPA from the region in **B**; **C** High-magnification Bright field STEM image, showing a high density of dislocations and SRCs; **D** Bright field STEM image and EDS element maps, indicating the significant Zr element segregation

4.3 Formation process of KB

Microstructure characterization reveals the presence of abundant KBs during the deformation of TiZrNbVTa RHEA under varying temperature and strain rate conditions. KBs are typically activated within highly localized plastic deformation zones [91].

According to Hess and Barrett [75], the activation of KB originates from lattice rotation induced by dislocation glide [70]. When normal dislocation motion in the slip direction is impeded on the slip plane, lattice rotation occurs around the Taylor axis to relieve the long-range stress field induced by dislocation accumulation [92]. In addition, due to the increased atomic disorder near GBs compared to the grain interior, the interatomic bonding is weaker, rendering it more susceptible to initiate preferential bending under substantial overlapping stress. As a result, the observed KBs predominantly originate at GBs and subsequently propagate into the grain interior. The evolution of KB in TiZrNbVTa RHEA during deformation is illustrated in Fig. 12. As previously discussed, the generation of dislocation pairs with opposite signs contributes to KB nucleation. The dislocations with $<1\bar{1}1>$ slip direction align to from walls perpendicular to the $\{1\bar{1}2\}$ slip plane, relieving the long-range stress field. These walls evolve into pre-KB boundaries, which act as barriers to dislocation glide due to the presence of misorientations. As plastic strain rises, the accumulated dislocations cause the pre-KB boundaries to transform from LAGBs to HAGBs, thereby promoting the formation of KBs. During continuous grain rotation, KBs thicken through the coalescence of smaller KBs. Deformation is accommodated either by the initiation of new KBs or by the coalescence of existing ones [66], providing insight into the observed evolution of KBs.

Additionally, deformation temperature plays a crucial role in the formation of KBs. KBs are absent in hot-deformed sample where recrystallization occurs, primarily due to the strong correlation between deformation temperature and the ease of slip system activation [93]. At higher temperatures, the resistance to slip decreases across all slip systems, facilitating more uniform deformation. Conversely, when the deformation temperature is significantly below the recrystallization temperature, intense deformation inhomogeneity develops as slip system activation becomes more dependent on crystal orientation [67]. Thus, low-temperature deformation is a favorable factor for triggering kinking in BCC alloys.

Recently, investigations have shown that the kinking deformation mode not only facilitates local stress relaxation to enhance plastic deformation capability but also

improves strength through the formation of KB boundaries [7, 67, 94, 95]. On the one hand, the nucleation of KBs enables the local rearrangement of dislocations, mitigates stress concentration, and effectively accommodates shear strain, thereby improving the ductility of the TiZrNbVTa RHEA. On the other hand, KBs exhibit distinct plastic deformation capacities compared to the surrounding matrix within the same grain, generating back stress in either the matrix or the KBs, which may activate an additional hetero-deformation induced (HDI) strengthening mechanism [67]. Furthermore, the KBs boundaries can act as effective barriers to dislocation motion, as presented in Figs. 5, 7, and 9. This behavior significantly contributes to grain boundary strengthening, akin to the effect of mechanical twinning in face-centered cubic alloys [96]. These findings reveal the formation mechanisms of KB in the TiZrNbVTa RHEA and their important role in enhancing mechanical properties, which is crucial for designing future RHEAs with excellent mechanical performance.

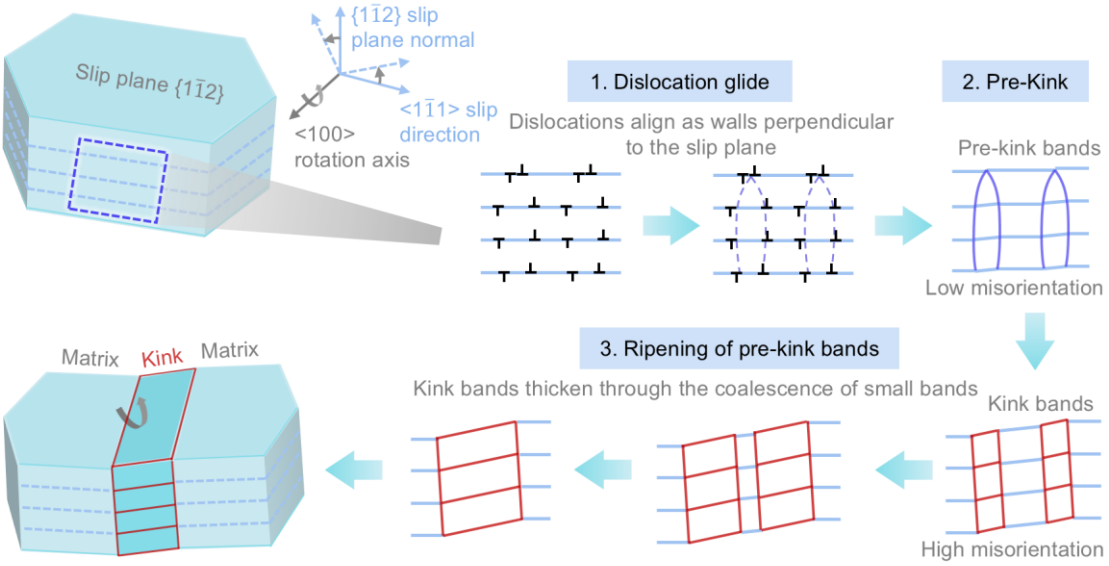

Fig. 12 Schematic diagram illustrating the process of KB formation in the TiZrNbVTa RHEA

4.4 SIMT from BCC to ω phase

The TEM analysis shown in Figs. 8, 10 confirms the SIMT from BCC to ω phase during high-strain-rate deformation of the TiZrNbVTa RHEA. The phase transformation, as a solid-state phase transition, plays a key role in modulating the

material properties [97, 98]. Understanding the transition from BCC phase to ω phase and how the transformation affects the properties of the TiZrNbVTa RHEA necessitates further investigation. The commonly recognized types of ω phase include: (1) deformation-induced ω phase, (2) athermal ω phase, and (3) isothermal ω phase [99]. The mechanism of ω phase formation is widely acted as the collapse of a pair of $\{111\}_{bcc}$ planes to an intermediate position, while leaving adjacent $\{111\}_{bcc}$ planes unaltered [100, 101]. The formation of the SIMT ω phase is a diffusionless transformation that introduces phase boundaries without causing compositional segregation. Due to the structural differences between the matrix and the ω phase, this process typically results in volume expansion and repartition of the stress/strain distribution in the grain [102], effectively enhancing the strain hardening of the TiZrNbVTa RHEA. This repartition promotes plastic deformation within grains, effectively suppressing early cracking [103]. Moreover, the newly formed ω phase introduces numerous interfaces that restrict dislocation propagation and motion. This suppression of crack formation, combined with the reduction in the mean free path of dislocations, results in a synergy of initial strain hardening and improved ductility.

4.5 Deformation mechanism over a wide range of temperatures and strain rates

Based on the microstructural analysis of the TiZrNbVTa RHEA deformed at various temperatures and strain rates, the corresponding deformation mechanisms are elucidated and schematically illustrated in Fig. 13. The initial TiZrNbVTa RHEA exhibits a single BCC phase and an equiaxed grain structure. The presence of KBs under varying conditions endows the RHEA with exceptional strength-ductility synergy, which is absent in hot-deformed samples due to the occurrence of DRX. Dislocation glide initiates the formation of KBs. As strain increases, dislocations pile-up and evolve into dislocation walls. The stress concentration induced by dislocation walls ultimately activates the KBs. At high strain rate, although the fundamental deformation mechanisms remain comparable, the SIMT from BCC to ω phase take place. The interphase boundary can act as effective barriers to dislocations motion. The

combined contributions of dislocation multiplication, KB deformation, and ω phase formation result in a stable strain-hardening rate, significantly enhancing the mechanical performance of the TiZrNbVTa RHEA. For the medium temperature range, the 3rd SA occurs, where moving dislocations are pinned by Zr-enriched SRCs. As temperature increases further, DRX occurs under quasi-static conditions, leading to pronounced thermal softening. With the increasing local strain, DRX regions expand and coalesce, resulting in shear localization.

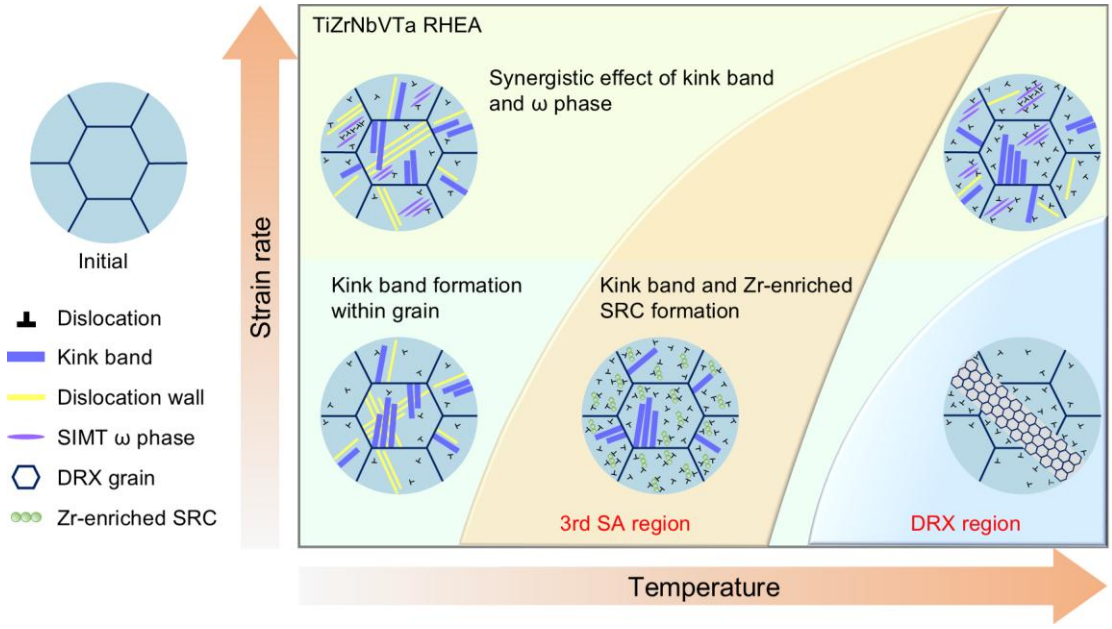

Fig. 13 Schematic diagram showing the deformation mechanisms of the TiZrNbVTa RHEA over a wide range of strain rates and temperatures

5. Conclusions

In this work, systemic compressive experiments over a wide range of temperatures (293 K – 1273 K) and strain rates (0.001 s^{-1} – 3000 s^{-1}) were performed to understand the mechanical behavior and deformation mechanisms of the TiZrNbVTa RHEA. Microstructure characterization and an in-depth discussion of the underlying mechanisms were conducted. These detailed and comprehensive studies provide valuable insights into the deformation mechanisms of RHEA systems. Findings of this study can be summarized as follows:

(1) The TiZrNbVTa RHEA shows an exceptional combination of strength and ductility over a wide range of temperatures and strain rates. It achieves a yield strength of approximately 1.3 GPa to 1.7 GPa at 293 K across strain rates from 0.001 s^{-1} to 3000 s^{-1}, while maintaining over 0.8 GPa even at a temperature of 1073 K and strain rate of 3000 s^{-1}.

(2) KBs are prominently observed in the deformed TiZrNbVTa RHEA. The formation of KBs progresses through dislocation gliding, pre-kinking, and the ripening of pre-KBs. At high strain rates, SIMT from BCC phase to ω phase is observed across different temperatures. The two main deformation modes not only promote local stress relaxation to enhance plastic deformation capability but also contribute to the strengthening of the RHEA.

(3) The 3rd SA occurs at different strain rates, shifting to a higher temperature range as strain rate increases. Zr atoms acting as "solute atoms" form SRCs at the moving dislocations. This produces a pinning effect, ultimately leading to the 3rd SA.

Statements and Declarations

The authors declare that they have no conflict of interest.

Ethical Standards

The experiments comply with the current laws of the country in which they were performed.

References

[1] Yeh JW, Chen SK, Lin SJ, Gan JY, Chin TS, Shun TT, Tsau CH, Chang SY. Nanostructured high-entropy alloys with multiple principal elements: novel alloy design concepts and outcomes. Adv Eng Mater. 2004;6(5): 299-303. https://doi.org/10.1002/adem.200300567.

[2] Cantor B, Chang I, Knight P, Vincent A. Microstructural development in equiatomic multicomponent alloys. Mater Sci Eng A. 2004;375: 213-8.https://doi.org/10.1016/j.msea.2003.10.257.

[3] Zuo Y, Fu Y, Xiong R, Sun L, Peng H, Wang H, Wen Y, Kim HS. From soft to ultrahard over 1000 HV: Engineering the hardness of FeMnAl(Cu) medium entropy alloys by unlocking the potential of β-Mn precipitation. Acta Mater. 2024;278: 120235.https://doi.org/10.1016/j.actamat.2024.120235.

[4] Li T, Liu T, Zhao S, Chen Y, Luan J, Jiao Z, Ritchie RO, Dai L. Ultra-strong tungsten refractory high-entropy alloy via stepwise controllable coherent nanoprecipitations. Nat Commun. 2023;14(1): 3006.https://doi.org/10.1038/s41467-023-38531-4.

[5] Yan Y-Q, Cha W-H, Liu S, Ma Y, Luan J-H, Rao Z, Liu C, Shan Z-W, Lu J, Wu G. Ductilization of 2.6-GPa alloys via short-range ordered interfaces and supranano precipitates. Science. 2025;387(6732): 401-6.https://doi.org/10.1126/science.adr4917.

[6] Wang K-Y, Cheng Z-J, Ning Z-L, Yu H-P, Ramasamy P, Eckert J, Sun J-F, Ngan AHW, Huang Y-J. Unraveling the cryogenic formability in high entropy alloy sheets under complex stress conditions. Rare Met. 2025;44(2): 1332-41.https://doi.org/10.1007/s12598-024-03075-z.

[7] Cook DH, Kumar P, Payne MI, Belcher CH, Borges P, Wang W, Walsh F, Li Z, Devaraj A, Zhang M. Kink bands promote exceptional fracture resistance in a NbTaTiHf refractory medium-entropy alloy. Science. 2024;384(6692): 178-84.https://doi.org/10.1126/science.adn2428.

[8] Gludovatz B, Hohenwarter A, Catoor D, Chang EH, George EP, Ritchie RO. A fracture-resistant high-entropy alloy for cryogenic applications. Science. 2014;345(6201): 1153-8.https://doi.org/10.1126/science.1254581.

[9] Feng R, Rao Y, Liu C, Xie X, Yu D, Chen Y, Ghazisaeidi M, Ungar T, Wang H, An K, Liaw PK. Enhancing fatigue life by ductile-transformable multicomponent B2 precipitates in a high-entropy alloy. Nat Commun. 2021;12(1): 3588.https://doi.org/10.1038/s41467-021-23689-6.

[10] Chen Y, Lu T, Lu H, Hu X, Yao N, Li K, Chen X, Bi Y, Sun B, Zhang X-C, Tu S-T. Lamellar microstructure enables exceptional fatigue resistance in a medium-entropy alloy manufactured by integrated directed energy deposition with interlayer rolling. Int J Plast. 2025;189: 104349.https://doi.org/10.1016/j.ijplas.2025.104349.

[11] Ren K, Liu H, Ma R, Chen S, Zhang S, Wang R, Chen R, Tang Y, Li S, Lu F. Dynamic compression behavior of TiZrNbV refractory high-entropy alloys upon ultrahigh strain rate loading. J Mater Sci Technol. 2023;161: 201-19.https://doi.org/10.1016/j.jmst.2023.04.008.

[12] Zhao S, Li Z, Zhu C, Yang W, Zhang Z, Armstrong DEJ, Grant PS, Ritchie RO, Meyers MA. Amorphization in extreme deformation of the CrMnFeCoNi high-entropy alloy. Sci Adv. 2021;7(5): eabb3108.https://doi.org/10.1126/sciadv.abb3108.

[13] Li W-Y, Wang M-L, Wang X-D, Wang T-M, Li T-J, Lu Y-P. A novel Co-free high-entropy alloy with excellent antimicrobial and mechanical properties. Rare Met. 2025;44(1): 581-90.https://doi.org/10.1007/s12598-024-02957-6.

[14] Yu X, Chen Q, Cui X, Ouyang D. Nb-induced lattice changes to enhance corrosion resistance of Al0.5Ti3Zr0.5NbxMo0.2 high-entropy alloys. Nat Commun. 2025;16(1): 2828.https://doi.org/10.1038/s41467-025-58211-9.

[15] Li B, Xia Y, Li H, Chen M, Wu Z, Tan X, Xu H. The study on the magnetic FeCoNiCuAl high-entropy alloy film with excellent corrosion resistance. Vacuum. 2025;232: 113859.https://doi.org/10.1016/j.vacuum.2024.113859.

[16] Zhang H-T, Wang C-L, Miao J-W, Shi S-Y, Li T-J, Yan H-W, Zhang Y-A, Lu Y-P. Effect of microstructure evolution on wear resistance of equal molar CoCrFeNi high-entropy alloy. Rare Met. 2023;42(11): 3797-805.https://doi.org/10.1007/s12598-023-02384-z.

[17] Abolkassem S, Elsayed A, Kariya S, Umeda J, Kondoh K. Microstructure, mechanical, and magnetic properties of powder metallurgy FeCoNiSi–Cu, FeCoNiSi–Mn, and FeCoNiSi-Ti equiatomic HEAs manufactured by spark plasma sintering. J Mater Res Technol. 2024;33: 9426-38.https://doi.org/10.1016/j.jmrt.2024.11.252.

[18] Ye YX, Liu CZ, Wang H, Nieh TG. Friction and wear behavior of a single-phase equiatomic TiZrHfNb high-entropy alloy studied using a nanoscratch technique. Acta Mater. 2018;147: 78-89.https://doi.org/10.1016/j.actamat.2018.01.014.

[19] San S, Adhikari P, Sakidja R, Brechtl J, Liaw PK, Ching W-Y. Porosity modeling in a TiNbTaZrMo high-entropy alloy for biomedical applications. RSC Adv. 2023;13(51): 36468-76.https://doi.org/10.1039/d3ra07313k.

[20] Qian B, Li X, Wang Y, Hou J, Liu J, Zou S, An F, Lu W. An Ultra-Low Modulus of Ductile TiZrHfTa Biomedical High-Entropy Alloys through Deformation Induced Martensitic Transformation/Twinning/Amorphization. Adv Mater. 2024;36(24): 2310926.https://doi.org/10.1002/adma.202310926.

[21] Gao M, Carney C, Doğan Ö, Jablonksi P, Hawk J, Alman D. Design of refractory high-entropy alloys. JOM. 2015;67: 2653-69.https://doi.org/10.1007/s11837-015-1617-z.

[22] Lilensten L, Couzinié J, Perrière L, Bourgon J, Emery N, Guillot I. New structure in refractory high-entropy alloys. Mater Lett. 2014;132: 123-5.https://doi.org/10.1016/j.matlet.2014.06.064.

[23] Senkov O, Wilks G, Miracle D, Chuang C, Liaw P. Refractory high-entropy alloys. Intermetallics. 2010;18(9): 1758-65.https://doi.org/10.1016/j.intermet.2010.05.014.

[24] Senkov ON, Miracle DB, Chaput KJ, Couzinie J-P. Development and

exploration of refractory high entropy alloys—A review. J Mater Res. 2018;33(19): 3092-128.https://doi.org/10.1557/jmr.2018.153.

[25] Praveen S, Kim HS. High-entropy alloys: potential candidates for high-temperature applications-an overview. Adv Eng Mater. 2018;20(1): 1700645. https://doi.org/10.1002/adem.201700645.

[26] Cao Y, Liu Y, Li Y, Liu B, Fu A, Nie Y. Precipitation behavior and mechanical properties of a hot-worked $TiNbTa_{0.5}ZrAl_{0.5}$ refractory high entropy alloy. Int J Refract Met Hard Mater. 2020;86: 105132.https://doi.org/10.1016/j.ijrmhm.2019.105132.

[27] Hua X, Hu P, Xing H, Han J, Ge S, Li S, He C, Wang K, Cui C. Development and property tuning of refractory high-entropy alloys: A review. Acta Metall Sin -Engl Lett. 2022;35(8): 1231-65.https://doi.org/10.1007/s40195-022-01382-x.

[28] Xiong W, Guo AXY, Zhan S, Liu C-T, Cao SC. Refractory high-entropy alloys: A focused review of preparation methods and properties. J Mater Sci Technol. 2023;142: 196-215.https://doi.org/10.1016/j.jmst.2022.08.046.

[29] Huang A, Fensin SJ, Meyers MA. Strain-rate effects and dynamic behavior of high entropy alloys. J Mater Res Technol. 2023;22: 307-47.https://doi.org/10.1016/j.jmrt.2022.11.057.

[30] Xiong W, Guo AX, Zhan S, Liu C-T, Cao SC. Refractory high-entropy alloys: A focused review of preparation methods and properties. J Mater Sci Technol. 2023;142: 196-215.https://doi.org/10.1016/j.jmst.2022.08.046.

[31] Wang R, Duan D, Tang Y, Lei Z, Li S, Chen R, Ma C, Wu Y, Bai S, Lu Z. Evading dynamic strength and ductility trade-off in a high-entropy alloy via local chemical ordering. Commun Mater. 2023;4(1): 25.https://doi.org/10.1038/s43246-023-00352-9.

[32] Wang Z, Zhou Y, Zheng H, Wang M, Li X, Li X, Li Z, Du Z, Xu L, Zhu Z. Mechanical response and deformation mechanism of Zr-Ti-Nb-Ta-Al refractory high-entropy alloy under the synergistic effects of temperature and strain rate. J Mater Sci Technol. 2025.https://doi.org/10.1016/j.jmst.2025.02.065.

[33] Zhang Z, Zhang H, Tang Y, Zhu La, Ye Y, Li S, Bai S. Microstructure, mechanical properties and energetic characteristics of a novel high-entropy alloy HfZrTiTa0.53. Mater Des. 2017;133: 435-43.https://doi.org/10.1016/j.matdes.2017.08.022.

[34] Hu M, Song W, Duan D, Wu Y. Dynamic behavior and microstructure characterization of TaNbHfZrTi high-entropy alloy at a wide range of strain rates and temperatures. Int J Mech Sci. 2020;182: 105738.https://doi.org/10.1016/j.ijmecsci.2020.105738.

[35] Dirras G, Couque H, Lilensten L, Heczel A, Tingaud D, Couzinié J-P, Perrière L, Gubicza J, Guillot I. Mechanical behavior and microstructure of $Ti_{20}Hf_{20}Zr_{20}Ta_{20}Nb_{20}$ high-entropy alloy loaded under quasi-static and dynamic compression conditions. Mater Charact. 2016;111: 106-13.https://doi.org/10.1016/j.matchar.2015.11.018.

[36] Zhang S, Wang Z, Yang H, Qiao J, Wang Z, Wu Y. Ultra-high strain-rate strengthening in ductile refractory high entropy alloys upon dynamic loading. Intermetallics. 2020;121: 106699.https://doi.org/10.1016/j.intermet.2020.106699.

[37] Laplanche G, Bonneville J, Varvenne C, Curtin WA, George EP. Thermal activation parameters of plastic flow reveal deformation mechanisms in the CrMnFeCoNi high-entropy alloy. Acta Mater. 2018;143: 257-64.https://doi.org/10.1016/j.actamat.2017.10.014.

[38] Zhang T, Jiao Z, Wang Z, Qiao J. Dynamic deformation behaviors and constitutive relations of an $AlCoCr_{1.5}Fe_{1.5}NiTi_{0.5}$ high-entropy alloy. Scr Mater. 2017;136: 15-9.https://doi.org/10.1016/j.scriptamat.2017.03.039.

[39] Couque H. The use of the direct impact Hopkinson pressure bar technique to describe thermally activated and viscous regimes of metallic materials. Philos Trans A Math Phys Eng Sci. 2014;372(2023): 20130218.https://doi.org/10.1098/rsta.2013.0218.

[40] Dirras G, Tingaud D, Csiszár G, Gubicza J, Couque H, Mompiou F.

Characterization of bulk bimodal polycrystalline nickel deformed by direct impact loadings. Mater Sci Eng A. 2014;601: 48-57.https://doi.org/10.1016/j.msea.2014.02.043.

[41] Wang R, Tang Y, Ai Y, Li S, Zhu La, Bai S. Strengthening and ductilization of a refractory high-entropy alloy over a wide strain rate range by multiple heterostructures. Int J Plast. 2024;173: 103882.https://doi.org/10.1016/j.ijplas.2024.103882.

[42] Xu D, Wang X, Lu Y. Heterogeneous-Structured Refractory High-Entropy Alloys: A Review of State-of-the-Art Developments and Trends. Adv Funct Mater. 2024;34(49): 2408941.https://doi.org/10.1002/adfm.202408941.

[43] Yasuda HY, Yamada Y, Cho K, Nagase T. Deformation behavior of HfNbTaTiZr high entropy alloy singe crystals and polycrystals. Mater Sci Eng A. 2021;809: 140983.https://doi.org/10.1016/j.msea.2021.140983.

[44] Dirras G, Gubicza J, Heczel A, Lilensten L, Couzinié JP, Perrière L, Guillot I, Hocini A. Microstructural investigation of plastically deformed Ti20Zr20Hf20Nb20Ta20 high entropy alloy by X-ray diffraction and transmission electron microscopy. Mater Charact. 2015;108: 1-7.https://doi.org/10.1016/j.matchar.2015.08.007.

[45] Couzinié JP, Lilensten L, Champion Y, Dirras G, Perrière L, Guillot I. On the room temperature deformation mechanisms of a TiZrHfNbTa refractory high-entropy alloy. Mater Sci Eng A. 2015;645: 255-63.https://doi.org/10.1016/j.msea.2015.08.024.

[46] Lee C, Maresca F, Feng R, Chou Y, Ungar T, Widom M, An K, Poplawsky JD, Chou Y-C, Liaw PK, Curtin WA. Strength can be controlled by edge dislocations in refractory high-entropy alloys. Nat Commun. 2021;12(1): 5474.https://doi.org/10.1038/s41467-021-25807-w.

[47] Maresca F, Curtin WA. Mechanistic origin of high strength in refractory BCC high entropy alloys up to 1900K. Acta Mater. 2020;182: 235-49.https://doi.org/10.1016/j.actamat.2019.10.015.

[48] Nemat-Nasser S, Isaacs J. Direct measurement of isothermal flow stress of metals at elevated temperatures and high strain rates with application to Ta and TaW alloys. Acta Mater. 1997;45(3): 907-19.https://doi.org/10.1016/S1359-6454(96)00243-1.

[49] Wang J, Guo W, Gao X, Su J. The third-type of strain aging and the constitutive modeling of a Q235B steel over a wide range of temperatures and strain rates. Int J Plast. 2015;65: 85-107.https://doi.org/10.1016/j.ijplas.2014.08.017.

[50] Lee C, Chou Y, Kim G, Gao MC, An K, Brechtl J, Zhang C, Chen W, Poplawsky JD, Song G. Lattice-distortion-enhanced yield strength in a refractory high-entropy alloy. Adv Mater. 2020;32(49): 2004029. https://doi.org/10.1002/adma.202004029.

[51] Brechtl J, Chen S, Lee C, Shi Y, Feng R, Xie X, Hamblin D, Coleman AM, Straka B, Shortt H. A review of the serrated-flow phenomenon and its role in the deformation behavior of high-entropy alloys. Metals. 2020;10(8): 1101.https://doi.org/10.3390/met10081101.

[52] Klose F, Ziegenbein A, Weidenmüller J, Neuhäuser H, Hähner P. Portevin–LeChatelier effect in strain and stress controlled tensile tests. Comput Mater Sci. 2003;26: 80-6.https://doi.org/10.1016/S0927-0256(02)00405-6.

[53] Kubin L, Estrin Y, Perrier C. On static strain ageing. Acta Metall Mater. 1992;40(5): 1037-44.https://doi.org/10.1016/0956-7151(92)90081-O.

[54] Bechtold JH. Tensile properties of annealed tantalum at low temperatures. Acta Metall. 1955;3(3): 249-54.https://doi.org/10.1016/0001-6160(55)90060-2.

[55] Chen S, Wang L, Li W, Tong Y, Tseng K, Tsai C, Yeh J, Ren Y, Guo W, Poplawsky J. Peierls barrier characteristic and anomalous strain hardening provoked by dynamic-strain-aging strengthening in a body-centered-cubic high-entropy alloy. Mater Res Lett. 2019;7(12): 475-81.https://doi.org/10.1080/21663831.2019.1658233.

[56] Antonaglia J, Xie X, Schwarz G, Wraith M, Qiao J, Zhang Y, Liaw PK, Uhl JT, Dahmen KA. Tuned critical avalanche scaling in bulk metallic glasses. Sci Rep.

2014;4(1): 4382.https://doi.org/10.1038/srep04382.

[57] Carroll R, Lee C, Tsai C, Yeh J, Antonaglia J, Brinkman BA, LeBlanc M, Xie X, Chen S, Liaw PK. Experiments and model for serration statistics in low-entropy, medium-entropy and high-entropy alloys. Sci Rep. 2015;5(1): 16997.https://doi.org/10.1038/srep16997.

[58] Zhang Y, Zuo TT, Tang Z, Gao MC, Dahmen KA, Liaw PK, Lu ZP. Microstructures and properties of high-entropy alloys. Prog Mater Sci. 2014;61: 1-93.https://doi.org/10.1016/j.pmatsci.2013.10.001.

[59] Rodriguez P. Serrated plastic flow. Bull Mater Sci. 1984;6: 653-63.https://doi.org/10.1007/BF02743993.

[60] Guo WG. Dynamic strain aging during the plastic flow of metals. Key Eng Mater. 2007;340: 823-8.https://doi.org/10.4028/www.scientific.net/KEM.340-341.823.

[61] Wang J, Guo H, Jiao Z, Zhao D, Chen X, Ma S, Zhang T, Liu X, Sha G, Qiao J, Brechtl J, Liaw PK, Wang Z. Coupling effects of temperature and strain rate on the mechanical behavior and microstructure evolution of a powder-plasma-arc additive manufactured high-entropy alloy with multi-heterogeneous microstructures. Acta Mater. 2024;276: 120147.https://doi.org/10.1016/j.actamat.2024.120147.

[62] Zhang L, Zhou J-T, Chen B-S, Wang Y, Ma Y-Z, Wang J, Huang Y-F, Liang C-P, Liu W-S. Composition redistribution-induced dynamic failure of dual-phase 90W-Ni–Fe alloy during adiabatic shear localization process. Rare Met. 2025;44(3): 1998-2010. https://doi.org/10.1007/s12598-024-03005-z.

[63] Kapoor R, Nemat-Nasser S. Determination of temperature rise during high strain rate deformation. Mech Mater. 1998;27(1): 1-12.https://doi.org/10.1016/S0167-6636(97)00036-7.

[64] Guo W, Gao X. On the constitutive modeling of a structural steel over a range of strain rates and temperatures. Mater Sci Eng A. 2013;561: 468-76.https://doi.org/10.1016/j.msea.2012.10.065.

[65] Nemat-Nasser S, Guo W, Liu M. Experimentally-based micromechanical modeling of dynamic response of molybdenum. Scr Mater. 1999;40(7): 859-72.https://doi.org/10.1016/S1359-6462(99)00041-X.

[66] Cui D, Bai X, Liu X, Qiu Y, Wang Z, Li J, Wang J, He F. Kinking induced plasticity in a novel refractory high-entropy alloy. Vacuum. 2024;227: 113424.https://doi.org/10.1016/j.vacuum.2024.113424.

[67] Luo W, Xue T, Zuo D, Cheng J, Liu Z, Liu H. Formation and strengthening mechanism of kink bands in an ultra-coarse-grained Fe-Cr-Al alloy. J Mater Sci Technol. 2024;186: 1-14.https://doi.org/10.1016/j.jmst.2023.11.017.

[68] Bertrand E, Castany P, Péron I, Gloriant T. Twinning system selection in a metastable β-titanium alloy by Schmid factor analysis. Scr Mater. 2011;64(12): 1110-3.https://doi.org/10.1016/j.scriptamat.2011.02.033.

[69] Yao HL, Yu YX, Sha JB. Microstructural evolution at grain boundary and deformation mechanism of $Nb_{0.5}TiZrV_{0.5}$ refractory high entropy alloy doped with Ce at room temperature. J Mater Sci Technol. 2024;196: 25-39.https://doi.org/10.1016/j.jmst.2024.01.046.

[70] Hagihara K, Mayama T, Honnami M, Yamasaki M, Izuno H, Okamoto T, Ohashi T, Nakano T, Kawamura Y. Orientation dependence of the deformation kink band formation behavior in Zn single crystal. Int J Plast. 2016;77: 174-91.https://doi.org/10.1016/j.ijplas.2015.10.005.

[71] Wang L, Sabisch J, Lilleodden ET. Kink formation and concomitant twin nucleation in Mg–Y. Scr Mater. 2016;111: 68-71.https://doi.org/10.1016/j.scriptamat.2015.08.016.

[72] Wang S, Wu M, Shu D, Sun B. Kinking in a refractory $TiZrHfNb_{0.7}$ medium-entropy alloy. Mater Lett. 2020;264: 127369.https://doi.org/10.1016/j.matlet.2020.127369.

[73] Li K, Chen W, Yu GX, Zhang JY, Xin SW, Liu JX, Wang XX, Sun J. Deformation kinking and highly localized nanocrystallization in metastable β-Ti alloys using cold forging. J Mater Sci Technol. 2022;120: 53-

64.https://doi.org/10.1016/j.jmst.2021.12.043.

[74] Luo W, Zuo D, Zhou H, Shen S, Zhang R, Liu H. Quasi in-situ investigation on kinking behavior of Fe-Cr-Al alloy during thermal compression. Mater Charact. 2023;204: 113225.https://doi.org/10.1016/j.matchar.2023.113225.

[75] Hess J, Barrett C. Structure and nature of kink bands in zinc. JOM. 1949;1: 599-606.https://doi.org/10.1007/BF03398902.

[76] Zhao B, Chen G, Lin Q, Wang K, Lv S, Fu X, Zhou W. Thermal deformation characteristics of $AlMo_{0.8}NbTiW_{0.2}Zr$ refractory multi-principal element alloy. Intermetallics. 2022;144: 107524.https://doi.org/10.1016/j.intermet.2022.107524.

[77] Alaneme KK, Anaele JU, Kareem SA. Hot deformability, microstructural evolution and processing map assessment of high entropy alloys: A systematic review. J Mater Res Technol. 2023;26: 1754-84.https://doi.org/10.1016/j.jmrt.2023.07.242.

[78] Eshelby JD. The determination of the elastic field of an ellipsoidal inclusion, and related problems. Proc Roy Soc Lond A. 1957;241(1226): 376-96.https://doi.org/10.1098/rspa.1957.0133.

[79] Xiao JF, Shang XK, Hou JH, Li Y, He BB. Role of stress-induced martensite on damage behavior in a metastable titanium alloy. Int J Plast. 2021;146: 103103.https://doi.org/10.1016/j.ijplas.2021.103103.

[80] Van Den Beukel A, Kocks UF. The strain dependence of static and dynamic strain-aging. Acta Metall. 1982;30(5): 1027-34.https://doi.org/10.1016/0001-6160(82)90211-5.

[81] Cottrell AH, Jaswon M. Distribution of solute atoms round a slow dislocation. Proc Roy Soc Lond A. 1949;199(1056): 104-14.https://doi.org/10.1098/rspa.1949.0128.

[82] Marchenko A, Mazière M, Forest S, Strudel J-L. Crystal plasticity simulation of strain aging phenomena in α-titanium at room temperature. Int J Plast. 2016;85: 1-33.https://doi.org/10.1016/j.ijplas.2016.05.007.

[83] Snoek JL. Tetragonal martensite and elastic after effect in iron. Physica. 1942;9(8): 862-4.https://doi.org/10.1016/S0031-8914(42)80061-0.

[84] Suzuki H. Chemical interaction of solute atoms with dislocations. Sci Rep Res Inst Tohoku Univ A. 1952;4: 455-63.http://hdl.handle.net/10097/26527.

[85] Chowdhury P, Sehitoglu H, Abuzaid W, Maier HJ. Mechanical response of low stacking fault energy Co–Ni alloys – Continuum, mesoscopic and atomic level treatments. Int J Plast. 2015;71: 32-61.https://doi.org/10.1016/j.ijplas.2015.04.003.

[86] Lee MH, Kim JH, Choi BK, Jeong YH. Mechanical properties and dynamic strain aging behavior of Zr–1.5Nb–0.4Sn–0.2Fe alloy. J Alloys Compd. 2007;428(1): 99-105.https://doi.org/10.1016/j.jallcom.2006.03.076.

[87] McCormigk PG. A model for the Portevin-Le Chatelier effect in substitutional alloys. Acta Metall. 1972;20(3): 351-4.https://doi.org/10.1016/0001-6160(72)90028-4.

[88] Xia Y, Lyu S, Li W, Chen Y, Ngan AHW. Defect-induced inhomogeneous atomic environments in complex concentrated alloys. Int J Plast. 2023;169: 103719.https://doi.org/10.1016/j.ijplas.2023.103719.

[89] Maiti S, Steurer W. Structural-disorder and its effect on mechanical properties in single-phase TaNbHfZr high-entropy alloy. Acta Mater. 2016;106: 87-97.https://doi.org/10.1016/j.actamat.2016.01.018.

[90] Blavette D, Cadel E, Fraczkiewicz A, Menand A. Three-Dimensional Atomic-Scale Imaging of Impurity Segregation to Line Defects. Science. 1999;286(5448): 2317-9.https://doi.org/10.1126/science.286.5448.2317.

[91] Li K, Zhao D, Xing Y, Chen W, Zhang J, Sun J. Kink-mediated high strength and large ductility via nanocrystallization in a tough titanium alloy. Acta Mater. 2024;273: 119963.https://doi.org/10.1016/j.actamat.2024.119963.

[92] Zheng Y, Zeng W, Wang Y, Zhang S. Kink deformation in a beta titanium alloy at high strain rate. Mater Sci Eng A. 2017;702: 218-24.https://doi.org/10.1016/j.msea.2017.07.015.

[93] Hull D. Orientation and temperature dependence of plastic deformation processes in 3·25% silicon iron. Proc Roy Soc Lond A. 1963;274(1356): 5-20.https://doi.org/10.1098/rspa.1963.0111.

[94] Somekawa H, Todaka Y, Ando D, Yuasa M. Kink bands strengthening of Mg-Y-Zn alloy via various wrought-processing. Mater Lett. 2021;304: 130653.https://doi.org/10.1016/j.matlet.2021.130653.

[95] Nakasuji Y, Somekawa H, Yuasa M, Miyamoto H, Yamasaki M, Kawamura Y. Quantitative kink boundaries strengthening effect of Mg-Y-Zn alloy containing LPSO phase. Mater Lett. 2021;292: 129625.https://doi.org/10.1016/j.matlet.2021.129625.

[96] Tu X, Wang J, Guo H, Zhao D, Jiao Z, Ma S, Wang R, Wang Q, Wang Z. Temperature effect on the microstructural refinement of equiatomic CoCrNi medium entropy alloy via cyclically multi-directional impact. J Alloys Compd. 2024;1003: 175722.https://doi.org/10.1016/j.jallcom.2024.175722.

[97] Zhang L, Narayan RL, Sun BA, Yan TY, Ramamurty U, Eckert J, Zhang HF. Cooperative Shear in Bulk Metallic Glass Composites Containing Metastable β-Ti Dendrites. Phys Rev Lett. 2020;125(5): 055501.https://doi.org/10.1103/PhysRevLett.125.055501.

[98] Chen H, Wang Y-D, Nie Z, Li R, Cong D, Liu W, Ye F, Liu Y, Cao P, Tian F, Shen X, Yu R, Vitos L, Zhang M, Li S, Zhang X, Zheng H, Mitchell JF, Ren Y. Unprecedented non-hysteretic superelasticity of [001]-oriented NiCoFeGa single crystals. Nat Mater. 2020;19(7): 712-8.https://doi.org/10.1038/s41563-020-0645-4.

[99] Ballor J, Li T, Prima F, Boehlert CJ, Devaraj A. A review of the metastable omega phase in beta titanium alloys: the phase transformation mechanisms and its effect on mechanical properties. Int Mater Rev. 2023;68(1): 26-45.https://doi.org/10.1080/09506608.2022.2036401.

[100] Lai MJ, Tasan CC, Zhang J, Grabowski B, Huang LF, Raabe D. Origin of shear induced β to ω transition in Ti–Nb-based alloys. Acta Mater. 2015;92: 55-

63.https://doi.org/10.1016/j.actamat.2015.03.040.

[101] Yang Y, Castany P, Bertrand E, Cornen M, Lin JX, Gloriant T. Stress release-induced interfacial twin boundary ω phase formation in a β type Ti-based single crystal displaying stress-induced α" martensitic transformation. Acta Mater. 2018;149: 97-107.https://doi.org/10.1016/j.actamat.2018.02.036.

[102] Liu L, He B, Huang M. The role of transformation-induced plasticity in the development of advanced high strength steels. Adv Eng Mater. 2018;20(6): 1701083.https://doi.org/10.1002/adem.201701083.

[103] Wang L, Fu C, Wu Y, Wang Q, Hui X, Wang Y. Formation and toughening of metastable phases in TiZrHfAlNb medium entropy alloys. Mater Sci Eng A. 2019;748: 441-52.https://doi.org/10.1016/j.msea.2018.12.033.